Quasi-static finite element modeling of seismic attenuation and dispersion due to wave-induced fluid flow in poroelastic media

Beatriz Quintal,[1] Holger Steeb,[2] Marcel Frehner,[3] and Stefan M. Schmalholz[1,4]

Received 15 February 2010; revised 17 September 2010; accepted 11 October 2010; published 4 January 2011.

[1] The finite element method is used to solve Biot's equations of consolidation in the displacement-pressure ($u - p$) formulation. We compute one-dimensional (1-D) and two-dimensional (2-D) numerical quasi-static creep tests with poroelastic media exhibiting mesoscopic-scale heterogeneities to calculate the complex and frequency-dependent P wave moduli from the modeled stress-strain relations. The P wave modulus is used to calculate the frequency-dependent attenuation (i.e., inverse of quality factor) and phase velocity of the medium. Attenuation and velocity dispersion are due to fluid flow induced by pressure differences between regions of different compressibilities, e.g., regions (or patches) saturated with different fluids (i.e., so-called patchy saturation). Comparison of our numerical results with analytical solutions demonstrates the accuracy and stability of the algorithm for a wide range of frequencies (six orders of magnitude). The algorithm employs variable time stepping and an unstructured mesh which make it efficient and accurate for 2-D simulations in media with heterogeneities of arbitrary geometries (e.g., curved shapes). We further numerically calculate the quality factor and phase velocity for 1-D layered patchy saturated porous media exhibiting random distributions of patch sizes. We show that the numerical results for the random distributions can be approximated using a volume average of White's analytical solution and the proposed averaging method is, therefore, suitable for a fast and transparent prediction of both quality factor and phase velocity. Application of our results to frequency-dependent reflection coefficients of hydrocarbon reservoirs indicates that attenuation due to wave-induced flow can increase the reflection coefficient at low frequencies, as is observed at some reservoirs.

Citation: Quintal, B., H. Steeb, M. Frehner, and S. M. Schmalholz (2011), Quasi-static finite element modeling of seismic attenuation and dispersion due to wave-induced fluid flow in poroelastic media, *J. Geophys. Res.*, *116*, B01201, doi:10.1029/2010JB007475.

1. Introduction

[2] Attenuation of seismic waves in partially saturated, porous rocks is of great interest because it has been observed that oil and gas reservoirs frequently exhibit high attenuation [e.g., *Dasgupta and Clark*, 1998; *Rapoport et al.*, 2004], especially at low seismic frequencies [*Chapman et al.*, 2006]. *Korneev et al.* [2004] used laboratory and field data to show that attenuation can be related to an increase in reflectivity at low frequencies. *Goloshubin et al.* [2006] showed three examples of field data in which oil-rich reservoirs exhibit increased reflectivity at low seismic frequencies (around 10 Hz), and that using low-frequency imaging has a strong potential for predicting hydrocarbon content in reservoirs.

[3] At low seismic frequencies, wave-induced fluid flow on the mesoscopic scale is presumably the major cause of wave attenuation and velocity dispersion in a partially saturated, porous rock [e.g., *Norris*, 1993; *Johnson*, 2001; *Pride et al.*, 2004; *Carcione and Picotti*, 2006; *Müller et al.*, 2010]. The partially saturated rock is approximated as a poroelastic medium with regions fully saturated by one fluid and other regions fully saturated by another fluid, frequently referred to as patchy saturation. The mesoscopic scale of these regions (or patches) is the scale much larger than the pore size, but much smaller than the wavelength. Wave-induced fluid flow is caused by fluid pressure differences between these two regions. *White* [1975] and *White et al.* [1975] introduced for this mesoscopic-loss mechanism a three-dimensional (3-D) model of a water-saturated medium with spherical gas-saturated inclusions and a one-dimensional (1-D) layered model referred to as the inter-layer flow model, respectively (Figure 1). *Dutta and Odé* [1979a, 1979b] showed that wave-induced fluid flow can be modeled using Biot's equations [*Biot*, 1962] for wave

[1]Department of Earth Sciences, ETH Zurich, Zurich, Switzerland.
[2]Mechanics–Continuum Mechanics, Ruhr-University Bochum, Bochum, Germany.
[3]Department for Geodynamics and Sedimentology, University of Vienna, Vienna, Austria.
[4]Now at Institute of Geology and Paleontology, University of Lausanne, Lausanne, Switzerland.

0148-0227/11/2010JB007475

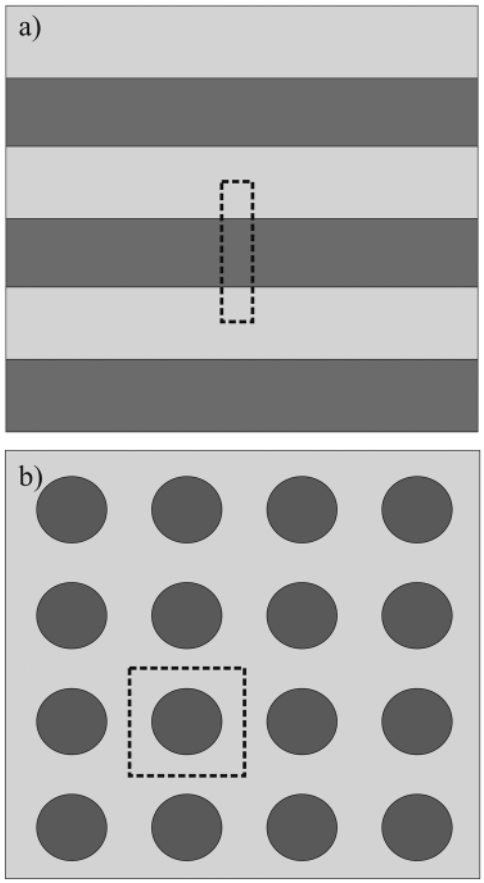

Figure 1. Sketches representing (a) a 1-D layered medium and (b) a 2-D medium with circular patches. The dashed boxes represent the numerical model domains used for the quasi-static experiments. The differently shaded areas indicate regions fully saturated with different fluids (i.e., patchy saturation).

propagation in poroelastic media with spatially varying petrophysical parameters.

[4] Theoretical studies based on White's model provide various closed-form analytical solutions for seismic attenuation in porous, saturated media with periodic mesoscopic-scale heterogeneities of particular geometries, such as layered media or media with spherical inclusions [e.g., *Johnson*, 2001; *Pride et al.*, 2004; *Vogelaar et al.*, 2010]. There are also analytical solutions for randomly layered media [e.g., *Gurevich and Lopatnikov*, 1995], but they are restricted to infinite media and to the type of autocorrelation function. *Müller and Gurevich* [2005] showed that significant differences in the magnitude and frequency dependence of attenuation are caused by the use of different autocorrelation functions. *Gurevich and Lopatnikov* [1995] showed that in the low-frequency limit, $1/Q$ (Q is the quality factor, and its inverse is a measure of attenuation) scales differently in infinite randomly layered media ($1/Q$ is proportional to the square root of frequency), compared to periodically layered media ($1/Q$ is proportional to frequency). However, for finite random media, $1/Q$ scales as in periodic media [*Müller and Rothert*, 2006; *Pride and Masson*, 2006]. Due to limitations of the analytical solutions, accurate numerical solutions for seismic attenuation in porous, saturated media with mesoscopic-scale heterogeneities are needed, for example, for heterogeneities with complicated geometries, presence of more than two heterogeneities such as patchy saturation involving more than two fluids, or finite random media with arbitrary distribution patterns.

[5] Many numerical schemes have been proposed for solving Biot's equations of wave propagation in heterogeneous poroelastic media [e.g., *Zhu and McMechan*, 1991; *Carcione and Quiroga-Goode*, 1995; *Dai et al.*, 1995; *Masson et al.*, 2006; *Wenzlau and Müller*, 2009]. However, calculating seismic attenuation due to wave-induced fluid flow with numerical algorithms for wave propagation in poroelastic media is computationally inefficient because wave propagation, fluid flow, and the diffusive fluid pressure response occur on significantly different time scales [e.g., *Carcione et al.*, 2003; *Masson et al.*, 2006; *Quintal et al.*, 2007]. A method that is computationally efficient in calculating attenuation due to wave-induced flow is a quasi-static creep test, as suggested by *Masson and Pride* [2007]. For the quasi-static creep test, they solved Biot's equations [*Biot*, 1962] for wave propagation in poroelastic media with a suitable finite difference algorithm [*Masson et al.*, 2006]. Recently, *Rubino et al*. [2009] and *Wenzlau et al.* [2010] have also presented quasi-static numerical strategies to calculate seismic attenuation due to wave-induced fluid flow. *Rubino et al*. [2009] computed oscillatory compressibility tests in the frequency domain to solve Biot's equations of wave propagation with the finite element method, and *Wenzlau et al.* [2010] computed quasi-static relaxation tests of numerical samples showing vertical transverse isotropy due to mesoscopic-scale heterogeneities using the finite element software Abaqus (Dassault Systèmes).

[6] In this study, we modified and elaborated the method suggested by *Masson and Pride* [2007]. As they did, we computed quasi-static creep tests for calculating seismic attenuation due to wave-induced fluid flow. However, (1) we solved a simpler mathematical problem, namely Biot's quasi-static equations of consolidation [*Biot*, 1941] in which inertial forces are excluded (Appendix A), and (2) we used the finite element method. Attenuation due to wave-induced fluid flow is controlled by the fluid pressure diffusion. For calculating attenuation due to only wave-induced fluid flow at low seismic frequencies, inertial forces are negligible [e.g., *Masson and Pride*, 2007], and it is sufficient to model only the related pressure diffusion. We used the finite element method [e.g., *Zienkiewicz and Taylor*, 1989; *Zienkiewicz et al.*, 1999] to solve Biot's equations of consolidation in the so-called $u - p$ formulation, where the equations are expressed in terms of the solid displacement, u, and fluid pressure, p. Our numerical scheme benefits from (1) consistent boundary conditions due to the $u - p$ formulation, including natural boundary conditions for no fluid flow; (2) an implicit solution for the time derivative allowing larger and especially variable time steps; (3) straightforward extension from one to two and three dimensions; (4) unstructured numerical meshes allowing the resolving of complicated geometries; and (5) no spatial derivatives of material parameters due to the finite element formulation, avoiding numerical inaccuracies caused by strong variations in material properties. We validated our 1-D and 2-D algorithms with an analytical solution and

theoretical high and low-frequency limits. The tests show that they are accurate over a wide frequency range.

[7] The main aims of this paper are to show (1), that the quasi-static creep test, described by Biot's equations of consolidation in the $u - p$ formulation and solved with the finite element method, is a powerful and accurate experiment for calculating attenuation and velocity dispersion due to wave-induced fluid flow and (2), that averages of White's analytical solution for periodic heterogeneities provide good estimates for attenuation and velocity dispersion in finite media with random distributions of sizes of heterogeneities in fluid saturation. For illustrating the implications of our study, we calculate the frequency-dependent reflection coefficient of a reservoir which exhibits attenuation and velocity dispersion due to wave-induced fluid flow between patches with randomly varying sizes.

2. Methodology of the Quasi-Static Creep Test

[8] We do numerical modeling of a quasi-static poroelastic experiment to compute the time-dependent strain response to a compressive total stress applied at the boundaries of a numerical rock sample with mesoscopic-scale heterogeneities [*Masson and Pride*, 2007]. Such a quasi-static experiment is called a creep test [e.g., *Lakes*, 2004]. The time-dependent stress-strain relation is used to calculate the frequency-dependent attenuation and velocity dispersion in the medium.

[9] In the 1-D interlayer flow model [*White et al.*, 1975], a partially saturated rock is represented by a poroelastic medium composed of two periodically alternating layers; each layer is fully saturated by one of two different fluids (Figure 1a). The smallest piece of the medium that can statistically represent the distribution of mesoscopic-scale heterogeneities within the entire medium is referred to as the representative elementary volume (REV). Its size is of the order of few to hundreds of mesoscopic-scale heterogeneities, depending on the distribution of heterogeneities. The (periodic) REV in the case of Figure 1a contains one pair of layers. For the numerical simulation (Appendix B), we chose the numerical rock sample to be the REV. Due to the mathematical formulation of the problem, we benefit from natural boundary conditions for the prescribed total stress and for fluid flow (equation (B7)) and we consider that the relative fluid velocity is zero on the boundary (undrained test). To be consistent with the undrained condition, the numerical rock sample is selected from the layered medium as shown by the dashed box in Figure 1a, because, due to symmetry, the fluid flow will be zero in the middle of the layers during the quasi-static experiment.

[10] With 1-D finite element modeling of Biot's quasi-static equations of consolidation (equation (B15)), we simulate a 1-D compression test by applying a total force on the top of the sample and setting the displacement at the bottom to zero. For that, we attribute a step function in time, $S(t)$, to the nodal component of $\boldsymbol{F}$ at the top of the sample, set all other nodal components of $\boldsymbol{F}$ to zero, including the ones corresponding to fluid flow, and set the nodal component of the solid displacement at the bottom to zero. The loading function, $S(t)$, is shown in Figure 2, normalized by its maximum value, $S^{\max}$. We use variable time steps, with small time increments at the beginning of the simulation, and larger time increments towards the end. Their length is linearly increased, whereby all time increments are numerically stable due to the implicit formulation. For visualization purposes, $S = 0$ for several of the first time steps, but it is sufficient to set $S = 0$ only at the first time step and $S = S^{\max}$ for all other time steps. For a porous medium, consisting of a homogeneous solid frame, partially saturated with water and gas (Figure 1a and Table 2), Figure 2 shows the relative fluid velocity, $\dot{w}_z$, and the fluid pressure, p, both normalized by their respective maximum values, at four stages of the creep test. The loading generates fluid pressure differences between regions saturated with different viscous fluids, and the less compressible fluid (water) flows into the region saturated with the more compressible fluid (gas), causing energy loss due to viscous dissipation.

[11] During the simulation, at each time step, (1) the total stress, σ_{zz}, and the strain, ε_{zz}, are calculated from the solid displacement, u_z, and fluid pressure, p; (2) their time derivatives, $\dot{\sigma}_{zz}$ and $\dot{\varepsilon}_{zz}$, i.e., the stress and strain rates, are calculated with a first order finite difference operator; and (3) the stress and strain rates are averaged (volume average) over the sample domain as

$$\overline{\dot{\sigma}_{zz}}(l) = \frac{1}{L}\sum_{n=1}^{N}\left(\int_n \dot{\sigma}_{zz}(l,n)dz(n)\right), \tag{1}$$

$$\overline{\dot{\varepsilon}_{zz}}(l) = \frac{1}{L}\sum_{n=1}^{N}\left(\int_n \dot{\varepsilon}_{zz}(l,n)dz(n)\right), \tag{2}$$

where l is the index of the time step, n is the element index, N is the number of elements, L is the length of the sample, and dz is the element length. Thus, at the end of the quasi-static simulation, we obtain the time evolution of the averaged stress and strain rates, $\overline{\dot{\sigma}_{zz}}(t)$ and $\overline{\dot{\varepsilon}_{zz}}(t)$, respectively. Applying a discrete Fourier transform to the averaged stress and strain rates, we obtain the complex and frequency-dependent values $\dot{\sigma}_{zz}(\omega)$ and $\dot{\varepsilon}_{zz}(\omega)$, where ω is the angular frequency. We use $\dot{\sigma}_{zz}(\omega)$ and $\dot{\varepsilon}_{zz}(\omega)$ to calculate the complex and frequency-dependent P wave modulus, $H(\omega)$.The P wave modulus is defined as

$$H = K_u + \frac{4}{3}\mu_u, \tag{3}$$

where K_u is the undrained bulk modulus and μ_u is the undrained shear modulus. For an isotropic sample, when the fractional change of fluid mass within the sample is zero (undrained condition), K_u and μ_u can be determined from

$$\dot{\sigma}_{ij}(\omega) = 2\mu_u(\omega)\left(\dot{\varepsilon}_{ij}(\omega) - \frac{1}{3}\dot{e}(\omega)\delta_{ij}\right) + K_u(\omega)\dot{e}(\omega)\delta_{ij} \tag{4}$$

[*Biot*, 1962; *Masson and Pride*, 2007]. For the 1-D case, equation (4) reduces to

$$\dot{\sigma}_{zz}(\omega) = \left(K_u(\omega) + \frac{4}{3}\mu_u(\omega)\right)\dot{\varepsilon}_{zz}(\omega), \tag{5}$$

therefore, using equation (5) in equation (3), $H(\omega)$ can be determined from the stress-strain ratio:

$$H(\omega) = \frac{\dot{\sigma}_{zz}(\omega)}{\dot{\varepsilon}_{zz}(\omega)}. \tag{6}$$

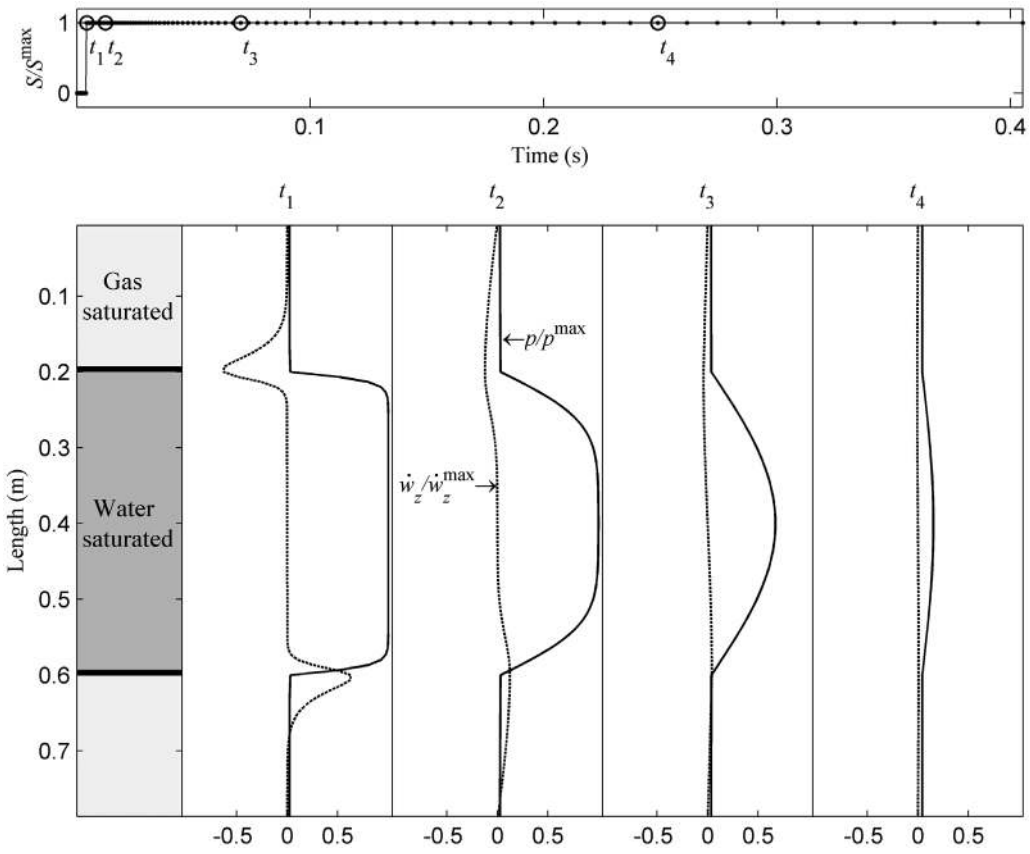

Figure 2. Four stages, t_1, t_2, t_3, and t_4, of the 1-D creep experiment (Figure 1a). A step function, S, is applied as a loading term at the top of the sample, and the solid displacement is set to zero at the bottom. The time evolution of S, normalized by its maximum value, S^{max}, is shown in the top graph. For visualization reasons, $S = 0$ at several of the first time steps. For each stage, the fluid velocity, $\dot{w}_z$ (dashed curve), and fluid pressure, p (solid curve), both normalized by their maximum values, are shown in the lower graphs.

The frequency-dependent quality factor is calculated from $H(\omega)$ as

$$Q(\omega) = \frac{\mathrm{Re}\{H(\omega)\}}{\mathrm{Im}\{H(\omega)\}}, \tag{7}$$

where Re and Im denote the real and imaginary parts, respectively. Attenuation is expressed as the inverse of quality factor, or $1/Q$. The complex and frequency-dependent P wave velocity is

$$V(\omega) = \sqrt{\frac{H(\omega)}{\rho}}, \tag{8}$$

where ρ is the bulk density of the partially saturated medium (material properties are defined in Table 1). The frequency-dependent phase velocity can be calculated from the complex velocity as

$$V_p(\omega) = \left(\mathrm{Re}\left\{\frac{1}{V(\omega)}\right\}\right)^{-1} \tag{9}$$

[e.g., *Carcione*, 2007]. The procedure for calculating the frequency-dependent values of Q and V from the time evolution of stress and strain is illustrated by *Wenzlau et al.* [2010, Figure 2].

[12] In two dimensions (equivalent to a 3-D case in which no strain out of the modeling plane is allowed to develop, i.e., plane strain), a partially saturated rock can be represented by a poroelastic medium fully saturated with one fluid, with circular regions fully saturated by another fluid (Figure 1b).

Table 1. Definitions of Symbols Used for the Petrophysical Parameters

Symbol	Petrophysical Parameter
k	Permeability
η	Viscosity of the fluid
ϕ	Porosity
μ	Shear modulus of the dry frame
K	Bulk modulus of the dry frame
K_s	Bulk modulus of the solid grains
K_f	Bulk modulus of the fluid
ρ	Bulk density of the saturated rock
ρ_s	Density of the solid grains
ρ_f	Density of the fluid
λ	$K - 2\mu/3$
α	$1 - K/K_s$
$\frac{1}{M}$	$\frac{\phi}{K_f} - \frac{\alpha - \phi}{K_s}$

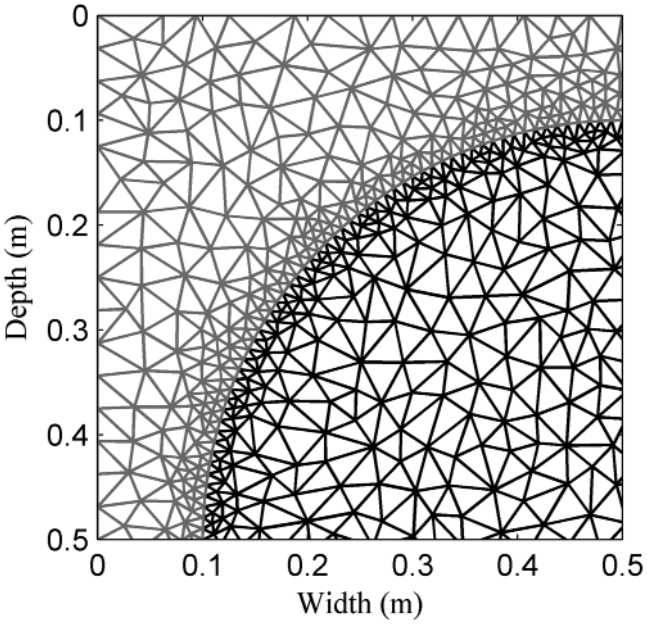

Figure 3. Zoom on the numerical mesh used for the 2-D simulations. Only a quarter of the entire grid is shown. The numerical model domain is a 1 m side square with a circular patch of 40 cm radius in the middle (dashed box in Figure 1b). Each triangular element of the unstructured mesh consists of seven nodal points (one on each corner, one in the middle of each side, and one in the middle of the triangle), on which the solid displacements and fluid pressure are calculated. Black and shaded lines are used for the mesh inside and outside the patch, respectively, where the elements have different petrophysical properties. The spatial resolution of the mesh can strongly vary.

For the numerical simulation (Appendix C), we chose the numerical rock sample to be the REV, and we selected it as a square with only one circular patch in the middle (dashed box in Figure 1b). The numerical rock sample is discretized with an unstructured triangular numerical mesh [*Shewchuk*, 1996, 2002] used in such a way that the material boundaries coincide with the element boundaries (Figure 3).

[13] We simulate a 2-D pure compression test by applying normal compressive total forces of equal magnitude at the four boundaries of the square sample. A time step function, $S(t)$ (Figure 4), is attributed to the nodal components of the loading term in the z direction at the top and bottom of the sample with opposite signs and, analogously, in the x direction. The step is not visible in Figure 4 because $S = 0$ only at the first step. We use variable time steps with linearly increasing increments towards the end of the simulation. For a gas-saturated rock with circular water-saturated regions (Figure 1b and Table 2), Figure 4 also shows the fluid pressure, p, and the relative fluid velocities in the x and z directions, $\dot{w}_x$ and $\dot{w}_z$, respectively, normalized by their maximum values at four stages of the simulation.

[14] During the simulation, at each time step, (1) the total stresses, σ_{zz}, σ_{xx} and σ_{xz}, and strains, ε_{zz}, ε_{xx} and ε_{xz}, are calculated from the solid displacements, u_z and u_x, and fluid pressure, p; (2) the time derivatives of their normal components, $\dot{\sigma}_{zz}$, $\dot{\sigma}_{xx}$, $\dot{\varepsilon}_{zz}$ and $\dot{\varepsilon}_{xx}$, i.e., the stress and strain rates, are calculated with a first-order finite difference operator; and (3) the stress and strain rates are averaged (volume average) over the sample domain as, for example,

$$\overline{\dot{\sigma}_{zz}}(l) = \frac{1}{A}\sum_{n=1}^{N}\left(\int_n \dot{\sigma}_{zz}(l,n)da(n)\right), \tag{10}$$

where A is the area of the sample, and da is the area of a triangular element. We obtain at the end of the simulation the time evolution of the averaged normal stress and strain rates, $\overline{\dot{\sigma}_{zz}}(t)$, $\overline{\dot{\sigma}_{xx}}(t)$, $\overline{\dot{\varepsilon}_{zz}}(t)$, and $\overline{\dot{\varepsilon}_{xx}}(t)$. Applying a discrete Fourier transform to the averaged normal stress and strain rates, we obtain $\dot{\sigma}_{zz}(\omega)$, $\dot{\sigma}_{xx}(\omega)$, $\dot{\varepsilon}_{zz}(\omega)$, and $\dot{\varepsilon}_{xx}(\omega)$, which are used to calculate the complex and frequency-dependent undrained bulk modulus, K_u (Appendix D). The quality factor associated with a pure undrained compression is

$$Q_{Ku}(\omega) = \frac{\mathrm{Re}\{K_u(\omega)\}}{\mathrm{Im}\{K_u(\omega)\}}. \tag{11}$$

3. Numerical Simulations and Results

3.1. Tests of the 1-D and 2-D Algorithms

[15] We test the 1-D numerical scheme for sandstone partially saturated with water and gas, represented by a poroelastic medium composed of two periodically alternating layers, fully saturated by one of the two fluids and having the same solid properties (Figure 1a). The thickness of the layers is 40 cm, and the petrophysical properties are given in Table 2. For the numerical simulation (Figure 2), each layer is divided into 60 finite elements and we use a total time of 0.41 s divided into 100 time increments of variable length. The total time was chosen as being one thousand times the thickness of the sample, divided by the phase velocity (from the analytical solution) at the frequency where the minimum Q occurs. With the presented algorithm, we obtain an excellent fit to the analytical solution of the 1-D interlayer flow model [e.g., *Carcione and Picotti*, 2006] shown in Figure 5. Roughly a quarter of the number of elements per layer used in this simulation is sufficient to yield a satisfactory fit with a slight deviation in the high-frequency limit in the $1/Q$ and V_p curves.

[16] We also test the 1-D numerical scheme for parameters representing a fractured rock, described as a layered 1-D model in which the fractures are very thin compliant layers of infinite extent, alternating with much thicker layers of a stiffer porous rock with lower permeability and porosity [e.g., *Gurevich et al.*, 2009]. We assume that the surrounding rock (i.e., the thicker layers) is saturated with water while the fractures are saturated with gas. This assumption is based on the fact that the wetting fluid, which is the water in this case, preferentially saturates regions of small pores due to capillary effects [*Goertz and Knight*, 1998]. The petrophysical parameters are given in Table 3. The REV consists of one pair of layers composed of one thin layer (5 mm thick) representing the fracture, and one thick layer (5 m thick) representing the surrounding rock. The numerical rock sample is the REV, selected similarly as for the first 1-D experiment (dashed box in Figure 1a), that is, from the middle of a thin gas-saturated layer to the middle of the next thin gas-saturated layer. The 5 mm layer

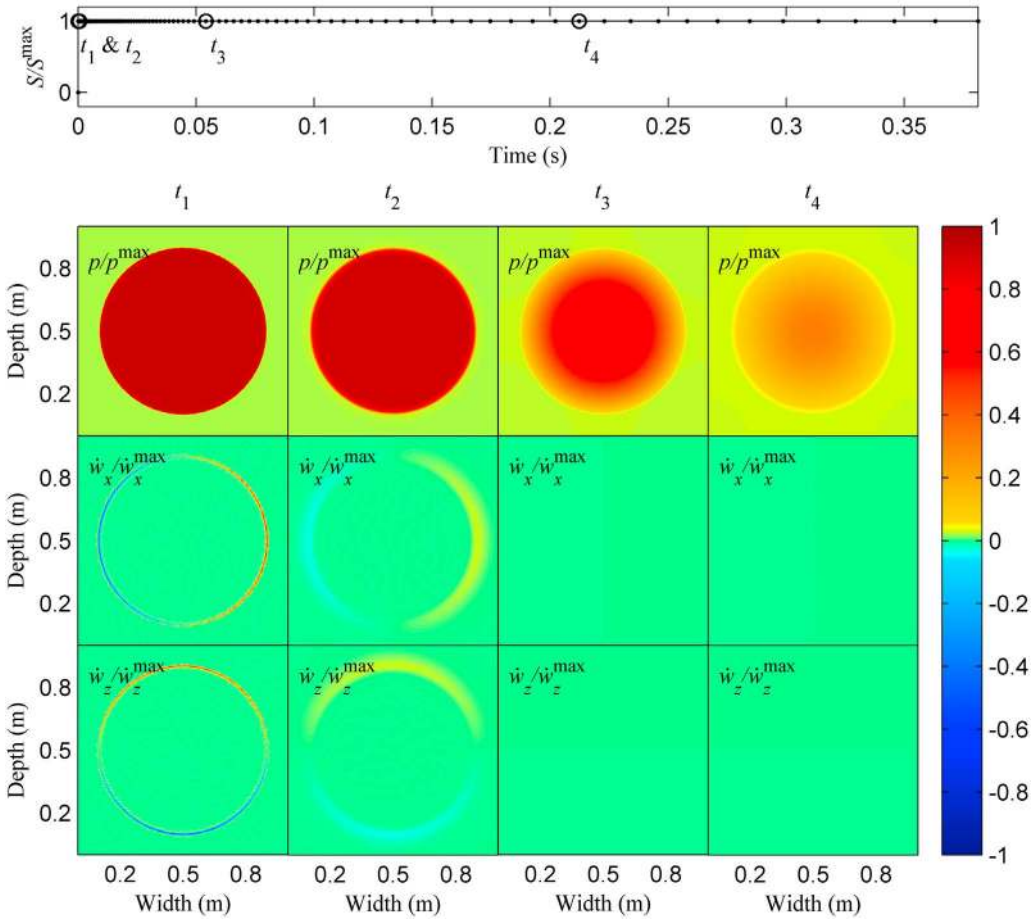

Figure 4. Four stages, t_1, t_2, t_3, and t_4, of the 2-D creep test (Figure 1b). A step function, S, is applied in the directions of normal compressive stresses at all the four boundaries of the square sample. The time evolution of S, normalized by its maximum value, S^{max}, is shown in the top graph. The step is not visible because $S = 0$ only at the first time step. For each stage, the fluid pressure, p, and the relative fluid velocities in x and z directions, $\dot{w}_x$ and $\dot{w}_z$, respectively, all normalized by their maximum values, are shown.

is divided into 20 elements and the 5 m layer into 400 elements. Larger layers are divided into more elements in order to keep the resolution relatively high close to the boundaries between layers, where most of the fluid flow occurs (e.g., see the curves for the relative fluid velocity in Figure 2). The total simulated time is 7.4 s, divided into 200 time increments with variable length. Figure 6 shows the numerical result for V_p and $1/Q$, together with the analytical solution of the 1-D interlayer flow model [e.g., *Carcione and Picotti*, 2006]. The considerable differences in thicknesses and petrophysical parameters of the two layers have a significant effect on a broad range of frequencies, compared to the simpler case of Figure 5. Our numerical scheme is able to reproduce the theoretically predicted intermediate asymptotic behavior of the frequency-dependent attenuation (i.e., $1/Q$) and still provides very accurate results in the low-frequency and high-frequency limits. Similar numerical simulations, such as the one from *Lambert et al.* [2006], who calculated Q from seismic wave propagation modeling in poroelastic media using reflectivity algorithms, are less accurate for low frequencies. This shows that the quasi-static finite element simulations are well suited when accurate results are required over a wide frequency range.

[17] The 2-D numerical scheme is tested for gas-saturated sandstone with circular water-saturated regions of identical solid properties (Figure 1b). The petrophysical properties are given in Table 2. The numerical rock sample is a square

Table 2. Petrophysical Parameters for the Benchmark Tests and for Examples of Media With Bimodal and Random Distributions of Sizes of Heterogeneities in Saturation

Rock-Matrix Parameters[a]	Sandstone	
k (mdarcy)	100	
ϕ	0.20	
μ (GPa)	3	
K (GPa)	4	
K_s (GPa)	40	
ρ_s (kg/m^3)	2700	
Rock-Fluid Parameters[a]	**Water**	**Gas**
K_f (GPa)	2.3	0.022
ρ_f (kg/m^3)	1000	140
η (Pa s)	0.003	10^{-5}

[a]Symbols are as defined in Table 1.

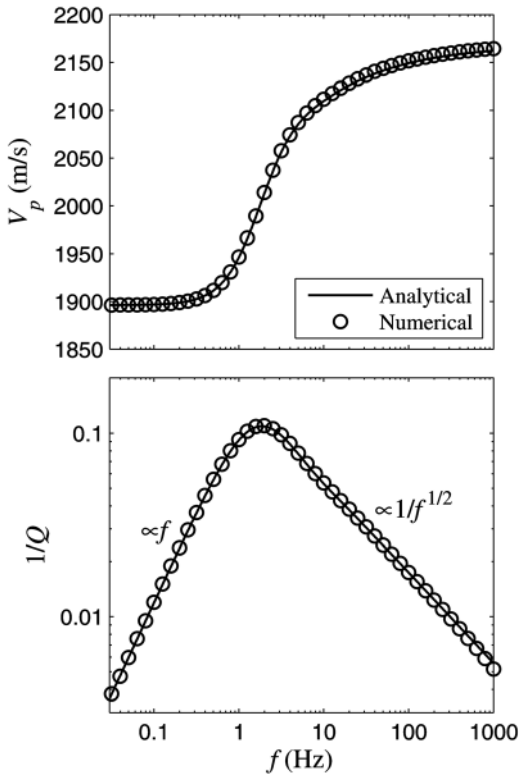

Figure 5. Test of the 1-D numerical scheme for a porous solid made of two periodically alternating fully saturated layers with water and gas (Figures 1a, 2, and Table 2). Each layer is 40 cm thick. Numerical and analytical results for the phase velocity, V_p, and inverse of quality factor, $1/Q$, are shown.

with one patch in the middle (dashed box in Figure 1b). The side of the square is 1 m and the radius of the circular patch is 40 cm. The spatial domain is divided into approximately 1200 triangular elements of variable area (Figure 3). This provides higher resolution close to the boundary of the patch, where most of the fluid flow takes place (see Figure 4). We use a total time of 0.39 s divided in 200 time increments of variable length. The total time was chosen as being eight hundred times the width of the numerical rock sample, divided by the average between the phase velocities calculated with Gassmann-Wood and Gassmann-Hill formulas [e.g., *Mavko et al.*, 1998; *Toms et al.*, 2006]. Figure 7 shows the numerical result for the real part of the undrained bulk modulus, $\mathrm{Re}\{K_u\}$, and for the inverse of the quality factor associated with a pure undrained compression, $1/Q_{Ku}$ (equation (11)). We check the result for $\mathrm{Re}\{K_u\}$ against its theoretical low-frequency and high-frequency limits (i.e., Gassmann-Wood and Gassmann-Hill limits), respectively. For $1/Q_{Ku}$, we show that the low and high-frequency asymptotes have the theoretically predicted frequency-dependent behavior [e.g., *Toms et al.*, 2006; *Masson and Pride*, 2007].

3.2. Rocks With Bimodal Distributions

[18] We investigate the effect of a bimodal distribution of sizes of mesoscopic-scale heterogeneities on the frequency-dependent quality factor and phase velocity of a poroelastic medium. In Figure 8, three layered media are shown, M1, M2, and M3. All consist of alternating sandstone layers saturated with water or gas (Table 2). Water and gas saturations are represented by black and white layers in M1 and M2. The thickness of the layers in M1 is 1 m, and in M2

Table 3. Petrophysical Parameters for the Example of a Fractured Rock

Rock-Matrix Parameters[a]	Surrounding Rock	Fractures
k (mdarcy)	100	1000
ϕ	0.10	0.20
μ (GPa)	5	3
K (GPa)	6	4
K_s (GPa)	40	40
ρ_s (kg/m^3)	2700	2700
Rock-Fluid Parameters[a]	**Water**	**Gas**
K_f (GPa)	2.3	0.022
ρ_f (kg/m^3)	1000	140
η (Pa s)	0.003	10^{-5}

[a]Symbols are as defined in Table 1.

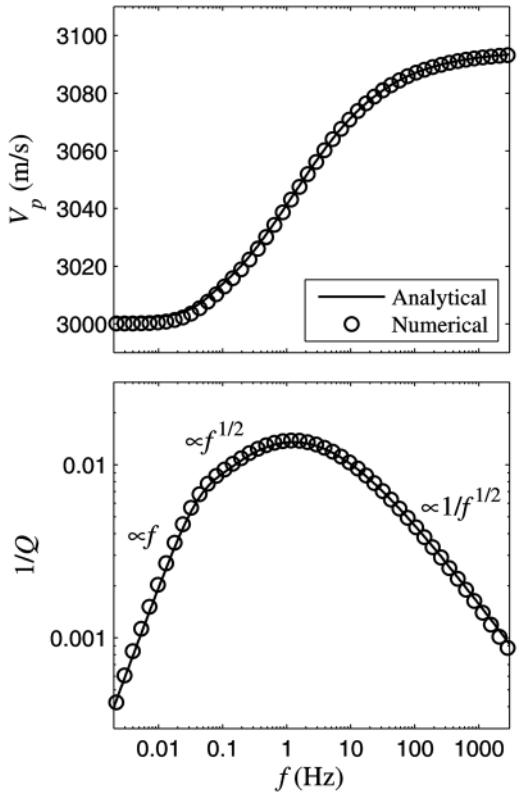

Figure 6. Result of the 1-D numerical simulation for a porous solid made of two periodically alternating fully saturated layers of very different thicknesses and petrophysical properties (Table 3), representing a fractured rock. The thicker layers (5 m) are saturated with water and the thinner layers (5 mm) with gas. Numerical and analytical results for the phase velocity, V_p, and inverse of quality factor, $1/Q$, are shown.

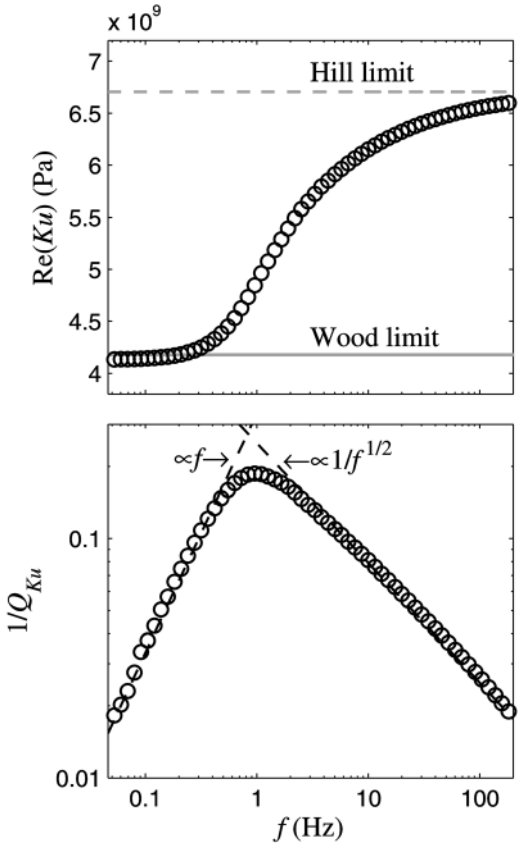

Figure 7. Test of the 2-D numerical scheme for the case of gas-saturated rock with circular water-saturated patches of 40 cm radius (Figures 1b, 3, and 4 and Table 2). The numerical results are the real part of the undrained bulk modulus, K_u, and the inverse of quality factor associated with a pure undrained compression, $1/Q_{Ku}$. Theoretical low-frequency and high-frequency limits of $\mathrm{Re}(K_u)$ and theoretically predicted variations of $1/Q_{Ku}$ with frequency are shown by dashed lines.

it is 10 cm. M3 represents a medium with a bimodal distribution of sizes of heterogeneities in saturation. It is composed of a combination of different portions of media M1 and M2 represented by light and dark grey layers in Figure 8. The stack of layers from M1 contains one pair of layers and is 2 m thick, and the stack of layers from M2 contains five pairs of layers and is 1 m thick. Analytical solution for the frequency-dependent elastic moduli is available for media with REV consisting of only one pair of layers, such as M1 and M2 [e.g., *Carcione and Picotti*, 2006]. The REV in M3 consists of one stack of layers from M1 and one stack of layers from M2. The numerical samples for M1 and M2 are the REV, selected as shown by the dashed box in Figure 1a. The numerical sample for M3 is also its REV, selected from the middle of the top layer in the stack from M1 to the middle of the top layer in the next stack from M1. A 1-D creep test is simulated as in the first experiment (Figures 1a and 2). The 10 cm layer is divided into 20 elements and the 1 m layer into 40 elements. The total simulated time is 4.4 s, divided into 200 time increments with variable length. The numerical parameters are the same for the three simulations, fulfilling all the time-space scale requirements of both M1 and M2; that is, the total time is long enough to resolve the low-frequency creep in M1, and the first time increments are small enough to resolve the higher-frequency creep process in M2. Therefore, the set of numerical parameters fulfills the time-space scale requirements of any combination of M1 and M2, such as M3. The numerical results are shown in Figure 9, together with the analytical solutions for M1 and M2 [e.g., *Carcione and Picotti*, 2006]. The numerical results for M1 and M2 agree well with the analytical solutions, from which we deduce that the numerical result for M3 is also accurate. The curves in Figure 9 suggest that the result for M3 can be predicted by a combination of the solutions for M1 and M2. To find an approximation for the response from M3, based on some combination of the analytical solutions for M1 and M2, we make an analogy between our poroelastic medium and a viscoelastic medium.

[19] A viscoelastic model commonly used to describe anelastic effects in rocks is the Zener model or standard linear solid model [*Zener*, 1948; *Carcione*, 2007]. The frequency-dependent complex P wave modulus of a poroelastic medium with mesoscopic-scale heterogeneities can be approximated using an equivalent Zener model [*Quintal et al.*, 2009]. By analogy, we assume that our poroelastic medium with bimodal distribution of mesoscopic-scale heterogeneities can be represented by a generalized Zener model composed of two Zener elements (i.e., having two inherent relaxation times). The two Zener elements have equivalent frequency-dependent behaviors to the poroelastic media M1 and M2. Analogous to the relationship between

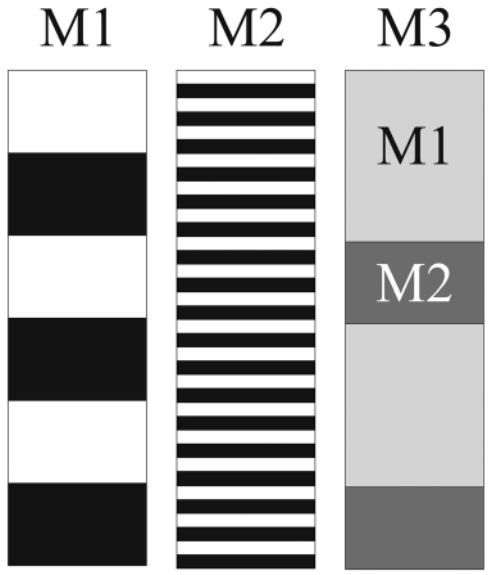

Figure 8. Models M1 and M2 represent layered media composed of two periodically alternating layers with different fluid saturation (Table 2). The layers in M1 are 1 m thick, and the layers in M2 are 10 cm thick (for visualization reasons, the layer thickness is exaggerated in M2, compared to the layer thickness in M1). M3 has a bimodal distribution of sizes of heterogeneities in saturation; it is composed of a combination of different portions of M1 and M2. The stack of layers from M1 in M3 is 2 m thick, and the stack of layers from M2 is 1 m thick.

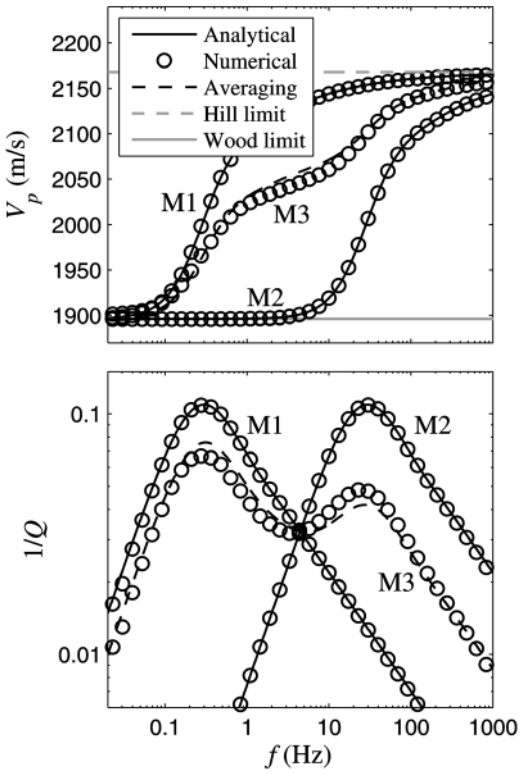

Figure 9. Numerical results for the layered media M1, M2, and M3 (Figure 8). The solid lines are the analytical solutions for media M1 and M2. The dashed, black lines refer to the results for M3b calculated with the averaging procedure given in equation (12). Gassmann-Wood and Gassmann-Hill limits for V_p are shown only for M3. The maximum attenuation in M1 occurs at 0.3 Hz and in M2 at 30 Hz.

the complex P wave modulus of the generalized Zener model and the complex P wave moduli of its elements, we suggest that the complex P wave modulus of the medium M3 can be calculated as volume averages of the moduli of its composing media M1 and M2:

$$\overline{H_3} = \frac{L_1 H_1 + L_2 H_2}{L_1 + L_2}, \tag{12}$$

where L_1 (=2 m) is the length of the stack of layers from M1 and L_2 (=1 m) is the length of the stack of layers from M2. The moduli H_1 and H_2 are the complex P wave moduli of M1 and M2, respectively, calculated with the analytical solution of the 1-D interlayer flow model [e.g., *Carcione and Picotti*, 2006]. The approximated result, $\overline{H_3}$, provides a good approximation to the numerical result (Figure 9). Because the length portion of M1 (66%) is greater than that of M2 (33%), the attenuation in M3 is significantly higher at the transition frequency of M1 than at the transition frequency of M2. Attenuation and dispersion in M3 are significant over a broad frequency range.

[20] The two stacks of different layer thicknesses in M3 had the same saturation ratio. We also test the approximation for a case in which the two stacks have different saturation ratios. We define M1b and M2b as media composed of two alternating layers saturated with water or gas (Table 2). In M1b the water-saturated layers are 1.5 m thick and the gas-saturated layers are 1 m thick. In M2b the water-saturated layers are 10 cm thick and the gas-saturated layers are 15 cm thick. The water saturation is 60% in M1b, and 40% in M2b. Two alternating stacks of layers from M1b and M2b compose the medium M3b. The stack from M1b contains one pair of layers and is 2.5 m thick, and the stack from M2b contains five pairs of layers and is 1.25 m thick. The 10 and 15 cm layers are divided into 20 elements and the 1 and 1.5 m layers into 40 elements. The total simulated time is 6.8 s, divided into 200 increments with variable length. The numerical results are shown in Figure 10, together with the analytical solutions for M1b and M2b [e.g., *Carcione and Picotti*, 2006], and the approximated solution for M3b (using equation (12)). The approximation fits the numerical result reasonably well despite the different saturation ratios in the two stacks composing M3b.

3.3. Rocks With Random Distributions

[21] We investigate the effect of a random distribution of sizes of mesoscopic-scale heterogeneities on the frequency-dependent elastic moduli of a finite poroelastic medium, and we test whether the approximation proposed in the last section can also be applied to a random distribution. We

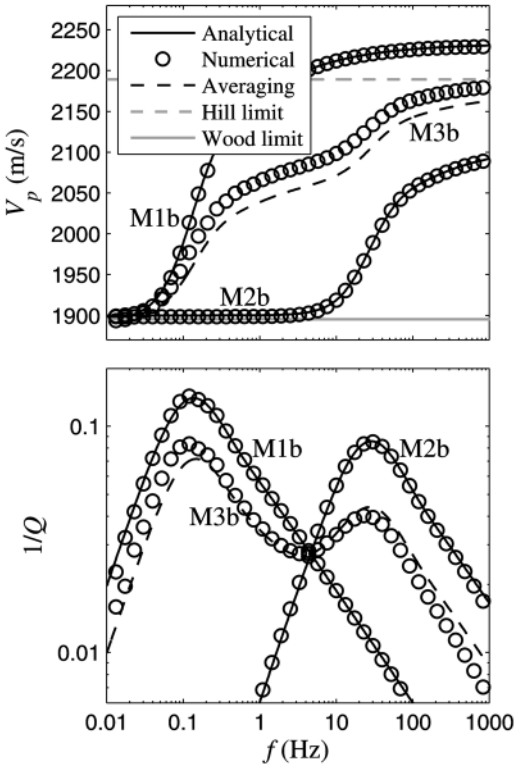

Figure 10. Numerical results for the layered media M1b, M2b, and M3b (see text). The solid lines are the analytical solutions for media M1b and M2b. The dashed, black lines refer to the results for M3b calculated with the averaging procedure given in equation (12). Gassmann-Wood and Gassmann-Hill limits for V_p are shown only for M3b. The maximum attenuation in M1b occurs at 0.14 Hz and in M2b at 29 Hz.

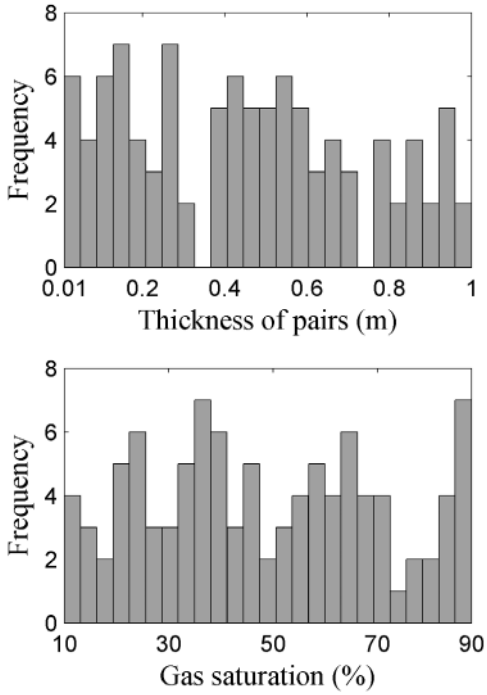

Figure 11. Frequency distribution of thicknesses of the one hundred pairs of layers and of values of gas saturation in those pairs. The minimum and maximum thicknesses of gas-saturated layers are 0.15 and 70 cm. The minimum and maximum thicknesses of water-saturated layers are 0.43 and 81 cm.

define our model as a layered medium consisting of one hundred pairs of layers, each pair composed of a fully gas-saturated layer on the top and a fully water-saturated layer on the bottom (Table 2). To build up the model, we generated one hundred thicknesses of pairs of layers randomly varying between 1 cm and 1 m, and one hundred values of gas saturation for such pairs randomly varying between S_{P1} = 10% and S_{P2} = 90%. We used the function *rand* from the software Matlab (MathWorks). Figure 11 shows histograms with the frequency distribution of thicknesses of pairs and the frequency distribution of values of gas saturation in the pairs. The overall gas saturation in the model is 46.4%, and the thicknesses of the 200 layers add to a total of 44.9 m. The numerical rock sample used for the quasi-static simulation is the entire model. The layers thinner than 5 cm are divided into 20 elements, the ones with thicknesses between 5 and 50 cm into 40 elements, and the ones thicker than 50 cm into 60 elements. The total simulated time is 9.2 s, divided into 200 time increments with variable length. The numerical results are shown in Figure 12, together with the theoretically predicted Gassmann-Wood and Gassmann-Hill limits for V_p [e.g., *Toms et al.*, 2006]. We observe that the low-frequency asymptote of $1/Q$ has the theoretically predicted behavior for finite random media [*Müller and Rothert*, 2006], that is, $1/Q$ is proportional to the frequency. For the averaging, the analytical solution of the 1-D interlayer flow model [e.g., *Carcione and Picotti*, 2006] is used for calculating the P wave modulus of each of the one hundred pairs of gas-saturated and water-saturated layers, and the P wave modulus of the model is approximated as

$$\overline{H} = \frac{\sum_{n=1}^{100} L_n H_n}{\sum_{n=1}^{100} L_n}, \tag{13}$$

where L_n is the thickness of the nth pair of layers having the complex P wave modulus H_n. The approximated result, $\overline{H}$, provides a good approximation to the numerical result (Figure 12).

[22] To quantify the accuracy of the averaging procedure given in equation (13), we use a systematic series of models. Each model is a layered medium consisting of one hundred pairs of layers with thicknesses randomly varying between 1 cm and 1 m. We use for all models the same set of pair thicknesses used in the last example (Figure 11). The difference between each model is the width of the random variation of gas saturation in those pairs; that is, all models have the same lower bound of gas saturation in the pairs, S_{P1} = 10%, but a different higher bound, S_{P2}. From model to model, S_{P2} varies from 15 to 90%. For such a variation of S_{P2}, the values of V_p at the low and high-frequency limits vary from 1924 to 1895 m/s and from 2453 to 2190 m/s, respectively, calculated with the theoretical Gassmann-

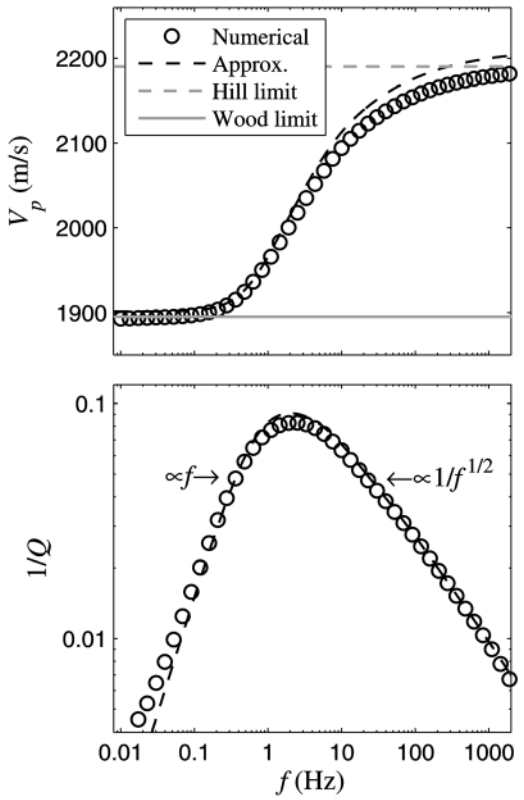

Figure 12. Numerical results and results calculated with the averaging procedure, equation (13), for the layered model with a random distribution of sizes of heterogeneities in saturation as described in Figure 13. Gassmann-Wood and Gassmann-Hill limits for V_p are also shown.

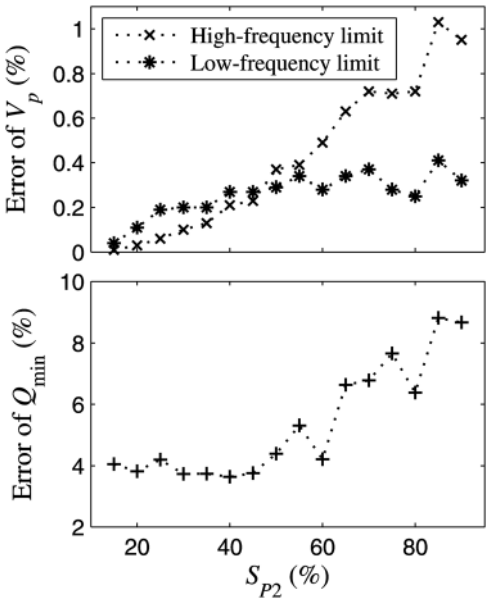

Figure 13. Relative error of V_p at the low-frequency and high-frequency limits and of the minimum value of Q (Q_{min}) calculated with the averaging procedure, equation (13), for a series of models consisting of the same one hundred pairs of layers with randomly varying thickness, but different widths of variation of gas saturation in those pairs. The gas saturation in the pairs varies from S_{P1} = 10% to S_{P2}. (The model with S_{P2} = 90% is the one shown in Figure 11, with V_p and $1/Q$ shown in Figure 12.) The error is plotted as a function of the higher bound of gas saturation in the pairs, S_{P2}. The errors of V_p at the low and high-frequency limits are relative to the respective theoretical Gassmann-Wood and Gassmann-Hill limits. The error of Q_{min} is relative to the numerically calculated value of Q_{min}.

Wood and Gassmann-Hill formulas [e.g., *Mavko et al.*, 1998; *Toms et al.*, 2006], and the value of the minimum value of Q or Q_{min}, and the frequency at which such minimum occurs vary from 6.7 to 12 Hz and from 1.2 to 2.2 Hz, respectively, calculated with numerical simulations. In Figure 13, we show the error of V_p at the low-frequency and high-frequency limits, approximated with equation (13), relative to the respective, exact values calculated with the theoretical Gassmann-Wood and Gassmann-Hill formulas. The relative error is the absolute value of the difference between approximated and exact values, divided by the exact value. We also show the error of Q_{min} approximated with equation (13), relative to the numerically calculated value of Q_{min}. In this case, the relative error is the absolute value of the difference between values calculated with equation (13) and with a numerical simulation, divided by the numerically calculated value. We observe in Figure 13 that the averaging procedure yields more accurate results for narrower variations of the saturation ratio. For variation of gas saturation in the pairs from S_{P1} = 10% to S_{P2} = 35%, the error of Q_{min} is lower than 5% and the error of V_p at both limits is around 0.2%. However, even for a wide variation of the saturation ratio in the pairs, such as S_{P1} = 10% to S_{P2} = 90% (Figure 11), the approximated results fits well the numerical results (Figure 12), with error of Q_{min} lower than 10% and error of V_p at both limits around 1% (Figure 13). This indicates that the simple approximation in equation (13) provides reasonably accurate predictions for both V_p and Q_{min} for partially saturated porous rocks with randomly varying patch sizes and saturations.

4. Discussion

[23] Biot's equations of consolidation have been solved with implicit finite element approaches in geomechanical engineering for many years [e.g., *Zienkiewicz and Taylor*, 1989; *Zienkiewicz et al.*, 1999]. We apply this well-established quasi-static finite element technique to creep simulations for calculating seismic attenuation and velocity dispersion in poroelastic media due to the mesoscopic-loss mechanism. Comparison of the numerical results with analytical solutions show that the algorithm is accurate and stable, and it is well suited to determine the complex moduli over a very broad frequency range (e.g., six orders of magnitude, as shown in Figure 6) and able to handle heterogeneities of very different sizes (e.g., three orders of magnitude, as in the example for a fractured rock). The algorithm is also fast, mainly because the time derivative is solved implicitly, allowing for larger and variable time increments. The fluid flow directly after the loading step at the beginning of the simulations (i.e., high frequencies) is accurately resolved with small time increments, and the pressure relaxation towards the end of the simulations (i.e., low frequencies) is resolved with much larger time increments. On a standard personal computer, the duration of the 1-D simulation (Figure 2) was less than 1 s and the 2-D simulation (Figure 4) was performed within a few minutes. Another advantage of the coupled ($u - p$) formulation are the boundary conditions for the pore fluid flow (drained/undrained) and for the total stress, which are fulfilled automatically due to the employed weak formulation. In addition, the extension from a 2-D algorithm to its 3-D version is straightforward in the finite element method and because of the unstructured mesh the finite element method is well suited for 2-D and 3-D simulations for numerical domains having complicated geometries [*Frehner and Schmalholz*, 2010].

[24] Furthermore, we applied an averaging procedure of analytical solutions for calculating attenuation and velocity dispersion in media with bimodal and random distributions of sizes of heterogeneities in saturation (equations (12) and (13), respectively). We showed that this approximation is accurate when the composing pairs of layers with different sizes exhibit approximately the same fluid saturation, and therefore the same average petrophysical properties. But the proposed averaging procedure is also suitable, with a small loss in accuracy, when the saturation ratio varies widely among pairs. When well logging data are available yielding information such as variation of fluid content and porosity with depth, this averaging procedure can be used to estimate the frequency-dependent quality factor and velocity dispersion (in the seismic range) of a finite rock unit.

[25] An important application of this work is to study and interpret low-frequency reflections. For example, the

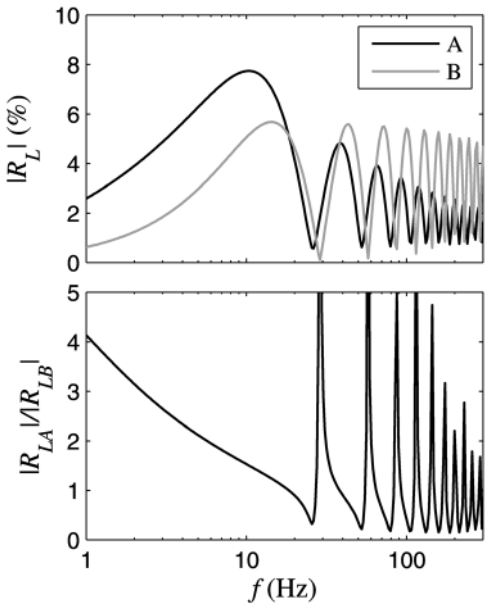

Figure 14. Absolute values of the normal-incidence reflection coefficients of a layer, R_L, in cases A and B, and their ratio, versus frequency. In case A, the layer is the model having gas saturation in the pairs randomly varying between S_{P1} = 10% and S_{P2} = 20% (Figure 13), that yields an overall gas saturation of 15%. The layer exhibits high attenuation and velocity dispersion at low seismic frequencies ($Q_{\min}$ = 6.7 at 1.2 Hz) due to wave-induced fluid flow. The complex P wave modulus is calculated with the averaging procedure, equation (13). In case B, the layer is fully saturated with water and presents constant and low attenuation (Q = 100). The thickness of the layer (h = 44.9 m) and the density and velocity in the nondispersive background medium are the same for both cases.

normal-incidence reflection coefficient of a layer is [e.g., *Brekhovskikh*, 1980]

$$R_L = \frac{1-z}{1+z}\left(1 - \frac{4zu}{(1+z)^2 - u(1-z)^2}\right), \qquad (14)$$

where $u = \exp(-2ih\omega)/V_2$, h is the thickness of the layer, and $z = V_2\rho_2/V_1\rho_1$ is the impedance ratio. Index 2 refers to the layer. Index 1 refers to the background medium where the layer is embedded (i.e., the half-spaces below and above the layer). We calculate the normal-incidence reflection coefficient of an attenuating layer that has the properties of one of the layered models discussed in the section 3.3 (Figure 13). The layer is the model having gas saturation in the pairs randomly varying between S_{P1} = 10% and S_{P2} = 20%. The overall gas saturation in the layer is 15%, and the overall density is 2334 kg/m^3. The thickness of the layer is h = 44.9 m. For V_2, we use the complex velocity of the layered model calculated with the averaging procedure, equation (13), and with equation (8). The complex velocity accounts for attenuation and velocity dispersion in the layer. The phase velocities in the low-frequency and high-frequency limits are 1915 and 2428 m/s, respectively, the minimum value of Q is 6.7 and occurs at around 1.2 Hz. For the background medium we consider a nondispersive shale with velocity equal to 2560 m/s (V_1) and density equal to 2250 kg/m^3. We refer to this example as case A. For comparison with case A, we calculate in case B the reflection coefficient of a layer which is fully saturated with water and presents constant and low attenuation (Q = 100). The properties of the rock matrix and of the water in the layer are the same as in case A (Table 2), yielding phase velocity equal to 2584 m/s (V_{2p}) and density equal to 2360 kg/m^3. To include the constant attenuation, we use for V_2 [*Carcione*, 2007]

$$V_2 = V_{2p}\left(1 - i\left(\sqrt{Q^2+1} - Q\right)\right)^{-1}. \qquad (15)$$

The thickness of the layer and the properties of the background medium are the same as in case A. In Figure 14 we show the magnitude or absolute value of R_L, denoted $|R_L|$, versus frequency for cases A and B. We also show the ratio between $|R_L|$ from case A and $|R_L|$ from case B. The oscillation of $|R_L|$ with frequency is due to tuning. Tuning is the effect of the positive and negative interferences of reflections from the top and bottom of the layer [e.g., *Kallweit and Wood*, 1982; *Liu and Schmitt*, 2003]. We observe that $|R_L|$ is approximately the same in cases A and B at about 20 Hz, but for lower frequencies the effect of high attenuation and velocity dispersion in case A yields larger values of $|R_L|$ than in case B. At 10 Hz, $|R_L|$ in case A is twice larger than in case B; at 2 Hz, $|R_L|$ in case A is three times larger than in case B.

[26] The comparison between (case A) the reflection coefficient of a water-saturated layer with patches of gas saturation (15%) exhibiting high attenuation and velocity dispersion caused by wave-induced fluid flow and (case B) a layer fully saturated with water exhibiting constant and low attenuation, shows that seismic wave attenuation and velocity dispersion can cause a significant increase in the reflection coefficient of a rock unit at low frequencies (Figure 14). This shows that the observations from *Goloshubin et al.* [2006] that oil-rich reservoirs exhibit increased reflectivity at low-frequencies (around 10 Hz), in comparison to the frequencies used by the conventional seismic industry (greater than 20 Hz), can be explained by high attenuation and velocity dispersion in those reservoirs.

[27] Although we only show P wave attenuation modeling, it is equally possible to model S wave attenuation by changing the loading setup in the 2-D (or 3-D) quasi-static experiment [*Masson and Pride*, 2007].

5. Conclusions

[28] We presented a numerical technique based on standard finite elements to calculate frequency-dependent attenuation and velocity dispersion in the seismic frequency range due to fluid flow in poroelastic media with mesoscopic-scale heterogeneities using a quasi-static creep test. The methodology for the quasi-static experiment is based on the work presented by *Masson and Pride* [2007], but instead of solving Biot's equations of wave propagation in porous

media [*Biot*, 1962] using the finite difference method, we solve Biot's quasi-static equations of consolidation [*Biot*, 1941] using the finite element method. Our alternative method provides additional benefits such as (1) more accurate calculations for heterogeneities having complicated, curved geometries due to the usage of unstructured mesh; (2), the simpler set of equations neglecting inertial effects increases the computational efficiency; (3) implicitly solving the time derivatives allows for larger and variable time increments, also increasing the computational efficiency; and (4) Biot's equations of consolidation written in the $u - p$ formulation provide natural boundary conditions for no fluid flow which are consistent to an undrained rock sample.

[29] Comparison of our 1-D and 2-D numerical results with analytical solutions shows that they are accurate over a wide range of frequencies. Our numerical scheme is well suited for modeling seismic attenuation and dispersion due to fluid flow in realistic media, such as 3-D rock samples with heterogeneities with complicated geometries and arbitrary distribution patterns. Additionally, rock and fluid properties can be varied independently and a larger number of different fluids (e.g., water, gas, and oil) can be modeled.

[30] We applied the numerical scheme to porous rocks with bimodal and random distributions of sizes of heterogeneities in fluid saturation. For such rocks, we proposed a volume average of analytical solutions for approximating the complex wave modulus. The approximate solutions yielded good fits to the numerical results. The proposed averaging method allows a fast, transparent and reasonably accurate prediction of the quality factor and P wave velocity in partially saturated porous rocks. Application of our results to reflection coefficients of hydrocarbon reservoirs suggests that the increased reflectivity at low frequencies, observed by, for example, *Goloshubin et al.* [2006], can be explained with frequency-dependent attenuation and velocity dispersion caused by wave-induced fluid flow.

Appendix A: The $u - p$ Formulation of Biot's Equations of Consolidation

[31] Neglecting body forces, Biot's quasi-static equations for a linear consolidation process [*Biot*, 1941] on the spatial domain $\Omega \in \mathbb{R}^d$, where d is the number of dimensions, over the time $\Im = [t_0, T]$ are

$$\begin{aligned} -\nabla \cdot \boldsymbol{\sigma} &= 0, \text{ in } \Omega \times \Im, \\ \nabla \cdot \left(-\frac{k}{\eta} \nabla p \right) + \alpha \nabla \cdot \dot{\boldsymbol{u}} + \frac{\dot{p}}{M} &= 0, \text{ in } \Omega \times \Im, \end{aligned} \tag{A1}$$

where a dot on the top of a variable represents the first partial time derivative and the symbol ∇ is the Nabla operator for spatial derivatives. The material properties k, η, α, and M are defined in Table 1. The symbol p represents the pore fluid pressure, $\boldsymbol{u}$ is the vector of solid displacement with its components u_i in the ith directions (e.g., for the full 3-D case $i = \{x, y, z\}$), and $\boldsymbol{\sigma}$ is the total stress tensor with components σ_{ij}. The boundary $\partial\Omega$ consists of the nonoverlapping Dirichlet part, $\Gamma_D^{f/s}$, and Neumann part, $\Gamma_N^{f/s}$, of the fluid and the solid frame (superscripts f and s, respectively), i.e., $\partial\Omega = \Gamma_D^{f/s} \cup \Gamma_N^{f/s}$ and $\Gamma_D^{f/s} \cap \Gamma_N^{f/s} = \emptyset$. The boundary conditions are given for p and $\boldsymbol{u}$ as

$$\begin{aligned} \boldsymbol{u} &= \overset{\smile}{\boldsymbol{u}} \text{ on } \Gamma_D^s, \\ p &= \overset{\smile}{p} \text{ on } \Gamma_D^f, \\ \boldsymbol{\sigma} \cdot \boldsymbol{n} &= \overset{\smile}{\boldsymbol{\tau}} \text{ on } \Gamma_N^s, \\ \dot{\boldsymbol{w}} \cdot \boldsymbol{n} &= \overset{\smile}{\dot{v}} \text{ on } \Gamma_N^f, \end{aligned} \tag{A2}$$

in which $\dot{\boldsymbol{w}}$ is the vector of the velocity of the fluid relative to the solid with its components $\dot{w}_i$ in the ith directions, $\boldsymbol{n}$ stands for the unit outward normal vector on the boundary, the symbols $\overset{\smile}{\boldsymbol{u}}$ and $\overset{\smile}{p}$ are the solid displacement vector and the fluid pressure, respectively, prescribed on the Dirichlet boundaries, and $\overset{\smile}{\boldsymbol{\tau}}$ and $\overset{\smile}{\dot{v}}$ are the stress vector and the fluid flow, respectively, prescribed on the Neumann boundaries. The associated initial conditions at time $t = t_0$ are given for p and $\boldsymbol{u}$ as

$$\begin{aligned} \boldsymbol{u} &= \boldsymbol{u}_0 \text{ at } \Omega \times t_0, \\ p &= p_0 \text{ at } \Omega \times t_0. \end{aligned} \tag{A3}$$

The velocity of the fluid relative to the solid is defined by Darcy's law

$$\dot{\boldsymbol{w}} = -\frac{k}{\eta} \nabla p, \tag{A4}$$

and the components σ_{ij} of the total stress tensor $\boldsymbol{\sigma}$ are [*Biot*, 1941, 1962]

$$\sigma_{ij} = 2\mu\varepsilon_{ij} + \lambda e \delta_{ij} - \alpha p \delta_{ij}, \tag{A5}$$

where δ_{ij} is the Kronecker delta, and μ and λ are the Lamé parameters defined in Table 1. The components of the strain tensor, ε_{ij}, are defined as

$$\varepsilon_{ij} = \frac{1}{2} \left(\frac{\partial u_i}{\partial x_j} + \frac{\partial u_j}{\partial x_i} \right) \tag{A6}$$

and the cubical dilatation, e, is given by the trace of the strain tensor

$$e = \sum_{i=1}^{n} \varepsilon_{ii}. \tag{A7}$$

Using the constitutive relations, equation (A5), for the total stress σ_{ij}, the system of equations (A1) can be expressed in terms of the two unknowns $\boldsymbol{u}$ and p and their derivatives in space and time, the so-called $u - p$ formulation [e.g., *Zienkiewicz and Shiomi*, 1984].

Appendix B: Finite Element Discretization Scheme (1-D)

[32] Biot's equations of consolidation, equations (A1), on the spatial domain $\Omega \in \mathbb{R}^1$ over the time $\Im = [t_0, T]$ are

$$\begin{aligned} -\frac{\partial \sigma_{zz}}{\partial z} &= 0, \text{ in } \Omega \times \Im, \\ -\frac{\partial}{\partial z} \left(\frac{k}{\eta} \frac{\partial p}{\partial z} \right) + \alpha \frac{\partial \dot{u}_z}{\partial z} + \frac{\dot{p}}{M} &= 0, \text{ in } \Omega \times \Im, \end{aligned} \tag{B1}$$

where σ_{zz} is the normal stress in the z direction. The boundary conditions are given for the fluid pressure, p, and for the solid displacement in the z direction, u_z, as

$$\begin{aligned} u_z &= \breve{u}_z \text{ on } \Gamma_D^s, \\ p &= \breve{p} \text{ on } \Gamma_D^f, \\ \frac{\partial}{\partial z}\sigma_{zz} &= \breve{\tau}_z \text{ on } \Gamma_N^s, \\ \frac{\partial}{\partial z}\dot{w}_z &= \breve{\upsilon}_z \text{ on } \Gamma_N^f, \end{aligned} \tag{B2}$$

where $\breve{u}_z$ and $\breve{p}$ are the solid displacement in the z direction and the fluid pressure, respectively, prescribed on the Dirichlet boundaries, and $\breve{\tau}_z$ and $\breve{\upsilon}_z$ are the normal stress and the fluid flow flux, respectively, prescribed on the Neumann boundaries. The initial conditions are given for p and u_z as

$$\begin{aligned} u_z &= u_{z0} \text{ at } \Omega \times t_0, \\ p &= p_0 \text{ at } \Omega \times t_0. \end{aligned} \tag{B3}$$

The normal stress in the z direction, σ_{zz}, using equations (A5) and (A6), is

$$\sigma_{zz} = (2\mu + \lambda)\frac{\partial u_z}{\partial z} - \alpha p. \tag{B4}$$

Substituting equation (B4) into equations (B1), the system of equations (B2) can be written in terms of the two unknowns, u_z and p (i.e., the $u - p$ formulation):

$$\begin{aligned} \frac{\partial}{\partial z}\left(-(2\mu + \lambda)\frac{\partial u_z}{\partial z} + \alpha p\right) &= 0, \\ -\frac{\partial}{\partial z}\left(\frac{k}{\eta}\frac{\partial p}{\partial z}\right) + \alpha\frac{\partial \dot{u}_z}{\partial z} + \frac{\dot{p}}{M} &= 0. \end{aligned} \tag{B5}$$

The 1-D initial boundary value problem given by equations (B1) is solved by the finite element method. Therefore, the equations are multiplied with test functions δu_z and δp and integrated over the spatial domain. Furthermore, the continuous functions u_z and p are approximated by u_{zh} and p_h and we introduce the shape functions N_i [e.g., *Zienkiewicz and Taylor*, 1989]. For a linear 1-D element consisting of two nodes (i.e., subscripts 1 and 2), the interpolated displacement and pressure are

$$\begin{aligned} u_{zh}(z) &\approx N_1(z)u_{zh1} + N_2(z)u_{zh2} = [N_1(z)\ N_2(z)]\begin{bmatrix} u_{zh1} \\ u_{zh2} \end{bmatrix} = \boldsymbol{N}\boldsymbol{u}_z, \\ p_h(z) &\approx N_1(z)p_{h1} + N_2(z)p_{h2} = [N_1(z)\ N_2(z)]\begin{bmatrix} p_{h1} \\ p_{h2} \end{bmatrix} = \boldsymbol{N}\boldsymbol{p}. \end{aligned} \tag{B6}$$

Note that the shape functions N_i are functions of z, while u_{zhi} and p_{hi} are the discrete nodal quantities. The resulting set of the discretized weak formulation in the domain R is

$$\begin{aligned} \int_R \left[\frac{\partial \boldsymbol{N}^T}{\partial z}(2\mu + \lambda)\frac{\partial \boldsymbol{N}}{\partial z}\boldsymbol{u}_z - \frac{\partial \boldsymbol{N}^T}{\partial z}\alpha\boldsymbol{N}\boldsymbol{p}\right]dr &= \int_{\partial R} \boldsymbol{N}^T\boldsymbol{N}\breve{\tau}_z dl, \\ \int_R \left[\frac{\partial \boldsymbol{N}^T}{\partial z}\frac{k}{\eta}\frac{\partial \boldsymbol{N}}{\partial z}\boldsymbol{p} + \boldsymbol{N}^T\alpha\frac{\partial \boldsymbol{N}}{\partial z}\dot{\boldsymbol{u}}_z + \boldsymbol{N}^T\frac{1}{M}\boldsymbol{N}\dot{\boldsymbol{p}}\right]dr &= -\int_{\partial R} \boldsymbol{N}^T\boldsymbol{N}\breve{\upsilon}_z dl. \end{aligned} \tag{B7}$$

We applied the Bubnov-Galerkin method, in which the test functions are chosen from the same function space as the shape functions [e.g., *Zienkiewicz and Taylor*, 1989]. $\boldsymbol{N}^T$ is the transpose of $\boldsymbol{N}$. Equations (B7) were integrated over a certain region R, bounded by ∂R. Applying Green's theorem, equations (B7) were integrated by parts according to convenient natural boundary conditions, expressed on the right-hand side. The right-hand side of the first equation of (B7) is the boundary term of the total stress applied at the boundary ∂R of the domain R. The right-hand side of the second equation in (B7) is the relative fluid velocity at the boundary ∂R of the region R.

[33] To solve this 1-D problem, equations (B7), for the unknown vectors $\boldsymbol{u}_z$ and $\boldsymbol{p}$, the components of the shape functions, $\boldsymbol{N}$, are defined as linear polynomial functions. For the local 1-D element (length dz) consisting of two end nodes, the components of $\boldsymbol{N}$ are

$$N_1 = 1 - \frac{z}{dz},\ N_2 = \frac{z}{dz}. \tag{B8}$$

The partial derivatives and integrals in equations (B7) can be solved analytically and the one-element problem can be written as

$$\boldsymbol{C}\dot{\boldsymbol{V}} + \boldsymbol{K}\boldsymbol{V} = \boldsymbol{F}, \tag{B9}$$

where $\boldsymbol{V}$ is the vector with the unknown components of $\boldsymbol{u}_z$ and $\boldsymbol{p}$,

$$\boldsymbol{V} = \begin{bmatrix} u_{z1} \\ p_1 \\ u_{z2} \\ p_2 \end{bmatrix}, \tag{B10}$$

$\boldsymbol{C}$ and $\boldsymbol{K}$ are the element damping matrix and element stiffness matrix, respectively,

$$\boldsymbol{C} = \begin{bmatrix} 0 & 0 & 0 & 0 \\ -\frac{\alpha}{2} & \frac{dz}{3M} & \frac{\alpha}{2} & \frac{dz}{6M} \\ 0 & 0 & 0 & 0 \\ -\frac{\alpha}{2} & \frac{dz}{6M} & \frac{\alpha}{2} & \frac{dz}{3M} \end{bmatrix}, \tag{B11}$$

$$\boldsymbol{K} = \begin{bmatrix} \frac{2\mu+\lambda}{dz} & \frac{\alpha}{2} & -\frac{2\mu+\lambda}{dz} & \frac{\alpha}{2} \\ 0 & \frac{k}{\eta dz} & 0 & -\frac{k}{\eta dz} \\ -\frac{2\mu+\lambda}{dz} & -\frac{\alpha}{2} & \frac{2\mu+\lambda}{dz} & -\frac{\alpha}{2} \\ 0 & -\frac{k}{\eta dz} & 0 & \frac{k}{\eta dz} \end{bmatrix}, \tag{B12}$$

and $\boldsymbol{F}$ is the vector containing the boundary terms expressed on the right-hand side of equations (B7). For the time derivative in equation (B9), we use a first-order finite difference operator,

$$\dot{\boldsymbol{V}} \approx \frac{\boldsymbol{V}^n - \boldsymbol{V}^o}{dt}, \tag{B13}$$

where superscripts n and o denote the value after (i.e., new) and before (i.e., old) a time increment, dt, respectively

[*Strang*, 1986]. Furthermore, we solve the system of equations (B9) implicitly,

$$\boldsymbol{C}\frac{\boldsymbol{V}^n-\boldsymbol{V}^o}{dt}+\boldsymbol{K}\boldsymbol{V}^n=\boldsymbol{F}, \tag{B14}$$

where $\boldsymbol{V}^n$ is the solution we seek:

$$\boldsymbol{V}^n=[\boldsymbol{C}+dt\boldsymbol{K}]^{-1}[\boldsymbol{C}\boldsymbol{V}^o+dt\boldsymbol{F}]. \tag{B15}$$

Appendix C: The 2-D Finite Element Scheme

[34] With Biot's equations of consolidation (equations (A1)) and the constitutive relations (equations (A2)) in the 2-D case, the equations of consolidation in the $u-p$ formulation are

$$\begin{Bmatrix} -\frac{\partial}{\partial x}\left((2\mu+\lambda)\frac{\partial u_x}{\partial x}+\lambda\frac{\partial u_z}{\partial z}\right)-\frac{\partial}{\partial z}\left(\mu\left(\frac{\partial u_x}{\partial z}+\frac{\partial u_z}{\partial x}\right)\right)+\frac{\partial}{\partial x}(\alpha p) \\ -\frac{\partial}{\partial z}\left((2\mu+\lambda)\frac{\partial u_z}{\partial z}+\lambda\frac{\partial u_x}{\partial x}\right)-\frac{\partial}{\partial x}\left(\mu\left(\frac{\partial u_x}{\partial z}+\frac{\partial u_z}{\partial x}\right)\right)+\frac{\partial}{\partial z}(\alpha p) \end{Bmatrix}=\begin{Bmatrix}0\\0\end{Bmatrix},$$
$$\frac{\partial}{\partial x}\left(-\frac{k}{\eta}\frac{\partial p}{\partial x}\right)+\frac{\partial}{\partial z}\left(-\frac{k}{\eta}\frac{\partial p}{\partial z}\right)+\alpha\left(\frac{\partial \dot{u}_x}{\partial x}+\frac{\partial \dot{u}_z}{\partial z}\right)+\frac{\dot{p}}{M}=0. \tag{C1}$$

The equations are multiplied with test functions δu_x, δu_z, and δp and integrated over the spatial domain. The continuous functions u_x, u_z, and p are approximated by the approximations u_{xh}, u_{zh}, and p_h and we introduce the shape functions N_{ui} and N_{pi} [e.g., *Zienkiewicz and Taylor*, 1989]

$$\begin{aligned} u_{xh}(x,z)&\approx \boldsymbol{N}_u(x,z)\boldsymbol{u}_x,\\ u_{zh}(x,z)&\approx \boldsymbol{N}_u(x,z)\boldsymbol{u}_z,\\ p_h(x,z)&\approx \boldsymbol{N}_p(x,z)\boldsymbol{p}. \end{aligned} \tag{C2}$$

The values of the unknowns at the element nodes are the components of vectors $\boldsymbol{u}_x$, $\boldsymbol{u}_z$, and $\boldsymbol{p}$: u_{xhi}, u_{zhi}, and p_{hi}, respectively. The shape functions for the displacements and fluid pressure, respectively, are the components of the matrices $\boldsymbol{N}_u$ and $\boldsymbol{N}_p$: N_{ui} and N_{pi}. Applying the Bubnov-Galerkin method, in which the test functions are chosen from the same function space as the shape functions, [e.g., *Zienkiewicz and Taylor*, 1989], we have the set of the discretized weak form

$$\int_R \begin{Bmatrix} \frac{\partial \boldsymbol{N}_u^T}{\partial x}\left((2\mu+\lambda)\frac{\partial \boldsymbol{N}_u}{\partial x}\boldsymbol{u}_x+\lambda\frac{\partial \boldsymbol{N}_u}{\partial z}\boldsymbol{u}_z\right)+\frac{\partial \boldsymbol{N}_u^T}{\partial z}\mu\left(\frac{\partial \boldsymbol{N}_u}{\partial z}\boldsymbol{u}_x+\frac{\partial \boldsymbol{N}_u}{\partial x}\boldsymbol{u}_z\right)-\frac{\partial \boldsymbol{N}_u^T}{\partial x}\alpha\boldsymbol{N}_p\boldsymbol{p} \\ \frac{\partial \boldsymbol{N}_u^T}{\partial z}\left((2\mu+\lambda)\frac{\partial \boldsymbol{N}_u}{\partial z}\boldsymbol{u}_z+\lambda\frac{\partial \boldsymbol{N}_u}{\partial x}\boldsymbol{u}_x\right)+\frac{\partial \boldsymbol{N}_u^T}{\partial x}\mu\left(\frac{\partial \boldsymbol{N}_u}{\partial z}\boldsymbol{u}_x+\frac{\partial \boldsymbol{N}_u}{\partial x}\boldsymbol{u}_z\right)-\frac{\partial \boldsymbol{N}_u^T}{\partial z}\alpha\boldsymbol{N}_p\boldsymbol{p} \end{Bmatrix} dr=\begin{Bmatrix}\int_{\partial R}\boldsymbol{N}_u^T\boldsymbol{N}_u\overset{\tau}{\smile}_x dl\\ \int_{\partial R}\boldsymbol{N}_u^T\boldsymbol{N}_u\overset{\tau}{\smile}_z dl\end{Bmatrix},$$
$$\int_R\left\{\frac{\partial \boldsymbol{N}_p^T}{\partial x}\frac{k}{\eta}\frac{\partial \boldsymbol{N}_p}{\partial x}\boldsymbol{p}+\frac{\partial \boldsymbol{N}_p^T}{\partial z}\frac{k}{\eta}\frac{\partial \boldsymbol{N}_p}{\partial z}\boldsymbol{p}+\boldsymbol{N}_p^T\alpha\left(\frac{\partial \boldsymbol{N}_u}{\partial x}\dot{\boldsymbol{u}}_x+\frac{\partial \boldsymbol{N}_u}{\partial z}\dot{\boldsymbol{u}}_z\right)+\boldsymbol{N}_p^T\frac{1}{M}\boldsymbol{N}_p\dot{\boldsymbol{p}}\right\}dr=-\left\{\int_{\partial R}\boldsymbol{N}_p^T\boldsymbol{N}_p\left(\overset{\dot{\upsilon}}{\smile}_x+\overset{\dot{\upsilon}}{\smile}_z\right)dl\right\}, \tag{C3}$$

where $\overset{\tau}{\smile}_x$, $\overset{\tau}{\smile}_z$, $\overset{\dot{\upsilon}}{\smile}_x$, and $\overset{\dot{\upsilon}}{\smile}_z$ are the normal stress in x and z directions, and the fluid flow flux in x and z directions, respectively, prescribed on the Neumann boundaries (equations (A2)). Equations (C3) were integrated over a certain region R, bounded by ∂R. Applying Green's theorem, they were integrated by parts according to convenient natural boundary conditions expressed on the right-hand side. The right-hand side of the first equation of (C3) is the boundary term of the total stress applied at the boundary ∂R of the domain R. The right-hand side of the second equation of (C3) is the relative fluid velocity at the boundary ∂R of the region R.

[35] The 2-D problem described by equations (C3) is solved as

$$\begin{bmatrix}\boldsymbol{G} & -\boldsymbol{Q}^T\\ 0 & \boldsymbol{H}\end{bmatrix}\begin{Bmatrix}\boldsymbol{u}\\ \boldsymbol{p}\end{Bmatrix}+\begin{bmatrix}0 & 0\\ \boldsymbol{Q} & \boldsymbol{S}\end{bmatrix}\begin{Bmatrix}\dot{\boldsymbol{u}}\\ \dot{\boldsymbol{p}}\end{Bmatrix}=\begin{Bmatrix}\boldsymbol{f}\\ \boldsymbol{q}\end{Bmatrix}\leftrightarrow \boldsymbol{K}\boldsymbol{V}+\boldsymbol{C}\dot{\boldsymbol{V}}=\boldsymbol{F}. \tag{C4}$$

In equation (C4), the vector $\boldsymbol{u}$ contains the discrete nodal values of $\boldsymbol{u}_x$ and $\boldsymbol{u}_z$ and $\boldsymbol{V}$ is a vector containing all unknowns (i.e., $\boldsymbol{u}_x$ and $\boldsymbol{u}_z$ and $\boldsymbol{p}$). The vector $\boldsymbol{f}$ contains the discrete nodal values of $\boldsymbol{f}_x$ and $\boldsymbol{f}_z$, and $\boldsymbol{F}$ is a vector containing the vector $\boldsymbol{f}$ and the vector $\boldsymbol{q}$. Matrices $\boldsymbol{K}$ and $\boldsymbol{C}$ are the element stiffness matrix and the element damping matrix, respectively, whose components are defined as

$$\begin{aligned} \boldsymbol{G}&=\int_R \boldsymbol{B}_{uG}^T\boldsymbol{D}\boldsymbol{B}_{uG}dr,\\ \boldsymbol{Q}&=\int_R \boldsymbol{N}_p^T\alpha\boldsymbol{B}_{uQ}dr,\\ \boldsymbol{H}&=\int_R \boldsymbol{B}_p^T\frac{k}{\eta}\boldsymbol{B}_p dr,\\ \boldsymbol{S}&=\int_R \boldsymbol{N}_p^T\frac{1}{M}\boldsymbol{N}^T dr. \end{aligned} \tag{C5}$$

In equations (C5), matrices $\boldsymbol{B}_{uG}$ and $\boldsymbol{B}_{uQ}$ contain the spatial derivatives of the displacement shape function $\boldsymbol{N}_u$ in a suitably organized way and matrix $\boldsymbol{B}_p$ contains the spatial derivatives of the pressure shape functions $\boldsymbol{N}_p$ in a suitably organized way [e.g., *Zienkiewicz and Taylor*, 1989].

[36] The actual element used in this study is an isoparametric 7-node triangular element [*Zienkiewicz and Taylor*, 1989]. The seven corresponding shape functions are biquadratic and continuous across element boundaries. We use the same set of shape functions for approximating displacements and pressure (i.e., $\boldsymbol{N}_u$ equal $\boldsymbol{N}_p$). The unstructured triangular numerical mesh is created by the software Triangle [*Shewchuk*, 1996, 2002] in such a way that the material boundaries coincide with the element boundaries. With this mesh, we are able to apply a variable resolution in the model domain to best suit the problem under consideration, that is, the resolution is high where the physical processes take place on a short length scale (i.e., close to the boundaries of heterogeneities) and lower elsewhere in the model domain. This provides both the best possible numerical accuracy and computational performance [*Frehner et al.*, 2008]. The integrals in equations (C5) are solved numerically using seven Gauss-Lobatto quadrature points [*Zienkiewicz and Taylor*, 1989].

[37] Finally, equation (C4) is discretized in time and solved using an implicit finite difference approach (equation (B15)).

Appendix D: Undrained Bulk Modulus for the 2-D Case

[38] In the 2-D case, using equation (4), $\dot{\sigma}_{zz}(\omega)$ and $\dot{\sigma}_{xx}(\omega)$ are

$$\dot{\sigma}_{zz}(\omega) = 2\mu_u(\omega)\dot{\varepsilon}_{zz}(\omega) + \left(K_u(\omega) - \frac{2}{3}\mu_u(\omega)\right)(\dot{\varepsilon}_{zz}(\omega) + \dot{\varepsilon}_{xx}(\omega)), \tag{D1}$$

$$\dot{\sigma}_{xx}(\omega) = 2\mu_u(\omega)\dot{\varepsilon}_{xx}(\omega) + \left(K_u(\omega) - \frac{2}{3}\mu_u(\omega)\right)(\dot{\varepsilon}_{zz}(\omega) + \dot{\varepsilon}_{xx}(\omega)). \tag{D2}$$

Adding equations (D1) and (D2), we obtain

$$K_u(\omega) = \frac{1}{2}\frac{\dot{\sigma}_{zz}(\omega) + \dot{\sigma}_{xx}(\omega)}{\dot{\varepsilon}_{zz}(\omega) + \dot{\varepsilon}_{xx}(\omega)} - \frac{1}{3}\mu_u(\omega), \tag{D3}$$

and subtracting equation (D2) from equation (D1), we obtain

$$\mu_u(\omega) = \frac{1}{2}\frac{\dot{\sigma}_{zz}(\omega) - \dot{\sigma}_{xx}(\omega)}{\dot{\varepsilon}_{zz}(\omega) - \dot{\varepsilon}_{xx}(\omega)}. \tag{D4}$$

Then, the undrained bulk modulus, $K_u(\omega)$, can be calculated with equations (D3) and (D4).

[39] **Acknowledgments.** This work was supported by ETH Zurich, the Swiss Innovation Promotion Agency (KTI/CTI), and Spectraseis. We thank Yuri Podladchikov for very constructive suggestions. Beatriz Quintal thanks Yolanda Deubelbeiss, Erik Saenger, and Marc-André Lambert for helpful input and discussions. Comments by three reviewers (two anonymous reviewers and Tobias Müller) and an associate editor are greatly appreciated.

References

Biot, M. A. (1941), General theory of three-dimensional consolidation, *J. Appl. Phys.*, *12*, 155–164, doi:10.1063/1.1712886.

Biot, M. A. (1962), Mechanics of deformation and acoustic propagation in porous media, *J. Appl. Phys.*, *33*, 1482–1498, doi:10.1063/1.1728759.

Brekhovskikh, L. M. (1980), *Waves in Layered Media*, 503 pp., Academic, New York.

Carcione, J. M. (2007), *Wave Fields in Real Media. Theory and Numerical Simulation of Wave Propagation in Anisotropic, Anelastic, Porous, and Electromagnetic Media*, 2nd ed., edited by K. Helbig and S. Treitel, Elsevier, Amsterdam.

Carcione, J. M., and S. Picotti (2006), *P* wave seismic attenuation by slow-wave diffusion: Effects of inhomogeneous rock properties, *Geophysics*, *71*, O1–O8, doi:10.1190/1.2194512.

Carcione, J. M., and G. Quiroga-Goode (1995), Some aspects of the physics and numerical modeling of Biot compressional waves, *J. Comput. Acoust.*, *3*, 261–280, doi:10.1142/S0218396X95000136.

Carcione, J. M., H. B. Helle, and N. H. Pham (2003), White's model for wave propagation in partially saturated rocks: Comparison with poroelastic numerical experiments, *Geophysics*, *68*, 1389–1398, doi:10.1190/1.1598132.

Chapman, M., E. Liu, and X. Li (2006), The influence of fluid-sensitive dispersion and attenuation on AVO analysis, *Geophys. J. Int.*, *167*, 89–105, doi:10.1111/j.1365-246X.2006.02919.x.

Dai, N., A. Vafidis, and E. R. Kanasewich (1995), Wave propagation in heterogeneous, porous media: A velocity-stress, finite-difference method, *Geophysics*, *60*, 327–340, doi:10.1190/1.1443769.

Dasgupta, R., and R. A. Clark (1998), Estimation of *Q* from surface seismic reflection data, *Geophysics*, *63*, 2120–2128, doi:10.1190/1.1444505.

Dutta, N. C., and H. Odé (1979a), Attenuation and dispersion of compressional waves in fluid-filled porous rocks with partial gas saturation (White model), Part I: Results, *Geophysics*, *44*, 1777–1788, doi:10.1190/1.1440938.

Dutta, N. C., and H. Odé (1979b), Attenuation and dispersion of compressional waves in fluid-filled porous rocks with partial gas saturation (White model), Part II: Results, *Geophysics*, *44*, 1789–1805, doi:10.1190/1.1440939.

Frehner, M., and S. M. Schmalholz (2010), Finite-element simulations of Stoneley guided-wave reflection and scattering at the tips of fluid-filled fractures, *Geophysics*, *75*, T23–T36, doi:10.1190/1.3340361.

Frehner, M., S. M. Schmalholz, E. H. Saenger, and H. Steeb (2008), Comparison of finite difference and finite element methods for simulating two-dimensional scattering of elastic waves, *Phys. Earth Planet. Inter.*, *171*, 112–121, doi:10.1016/j.pepi.2008.07.003.

Goertz, D., and R. Knight (1998), Elastic wave velocities during evaporative drying, *Geophysics*, *63*, 171–183, doi:10.1190/1.1444310.

Goloshubin, G., C. VanSchuyver, V. Korneev, D. Silin, and V. Vingalov (2006), Reservoir imaging using low frequencies of seismic reflections, *Leading Edge*, *25*, 527–531, doi:10.1190/1.2202652.

Gurevich, B., and S. L. Lopatnikov (1995), Velocity and attenuation of elastic waves in finely layered porous rocks, *Geophys. J. Int.*, *121*, 933–947, doi:10.1111/j.1365-246X.1995.tb06449.x.

Gurevich, B., M. Brajanovski, R. J. Galvin, T. M. Müller, and J. Toms-Stewart (2009), *P* wave dispersion and attenuation in fractured and porous reservoirs: Poroelasticity approach, *Geophys. Prospect.*, *57*, 225–237, doi:10.1111/j.1365-2478.2009.00785.x.

Johnson, D. L. (2001), Theory of frequency dependent acoustics in patchy-saturated porous media, *J. Acoust. Soc. Am.*, *110*, 682–694, doi:10.1121/1.1381021.

Kallweit, R. S., and L. C. Wood (1982), The limits of resolution of zero-phase wavelets, *Geophysics*, *47*, 1035–1046, doi:10.1190/1.1441367.

Korneev, V. A., G. M. Goloshubin, T. M. Daley, and D. B. Silin (2004), Seismic low-frequency effects in monitoring fluid-saturated reservoirs, *Geophysics*, *69*, 522–532, doi:10.1190/1.1707072.

Lakes, R. S. (2004), Viscoelastic measurement techniques, *Rev. Sci. Instrum.*, *75*, 797–810, doi:10.1063/1.1651639.

Lambert, G., B. Gurevich, and M. Brajanovski (2006), Attenuation and dispersion of *P* waves in porous rocks with planar fractures: Comparison of theory and numerical simulations, *Geophysics*, *71*, N41–N45, doi:10.1190/1.2197490.

Liu, Y., and D. R. Schmitt (2003), Amplitude and AVO responses of a single thin bed, *Geophysics*, *68*, 1161–1168, doi:10.1190/1.1598108.

Masson, Y. J., and S. R. Pride (2007), Poroelastic finite difference modeling of seismic attenuation and dispersion due to mesoscopic-scale heterogeneity, *J. Geophys. Res.*, *112*, B03204, doi:10.1029/2006JB004592.

Masson, Y. J., S. R. Pride, and K. T. Nihei (2006), Finite difference modeling of Biot's poroelastic equations at seismic frequencies, *J. Geophys. Res.*, *111*, B10305, doi:10.1029/2006JB004366.

Mavko, G., T. Mukerji, and J. Dvorkin (1998), *The Rock Physics Handbook: Tools for Seismic Analysis in Porous Media*, 329 pp., Cambridge Univ. Press, New York.

Müller, T. M., and B. Gurevich (2005), Wave-induced fluid flow in random porous media: Attenuation and dispersion of elastic waves, *J. Acoust. Soc. Am.*, *117*, 2732–2741, doi:10.1121/1.1894792.

Müller, T. M., and E. Rothert (2006), Seismic attenuation due to wave-induced flow: Why *Q* in random structures scales differently, *Geophys. Res. Lett.*, *33*, L16305, doi:10.1029/2006GL026789.

Müller, T. M., B. Gurevich, and M. Lebedev (2010), Seismic wave attenuation and dispersion resulting from wave-induced flow in porous rocks—A review, *Geophysics*, *75*, 75A147, doi:10.1190/1.3463417.

Norris, A. N. (1993), Low-frequency dispersion and attenuation in partially saturated rocks, *J. Acoust. Soc. Am.*, *94*, 359–370, doi:10.1121/1.407101.

Pride, S. R., and Y. J. Masson (2006), Acoustic attenuation in self-affine porous structures, *Phys. Rev. Lett.*, *97*, 184301, doi:10.1103/PhysRevLett.97.184301.

Pride, S. R., J. G. Berryman, and J. M. Harris (2004), Seismic attenuation due to wave-induced flow, *J. Geophys. Res.*, *109*, B01201, doi:10.1029/2003JB002639.

Quintal, B., S. M. Schmalholz, Y. Y. Podladchikov, and J. M. Carcione (2007), Seismic low-frequency anomalies in multiple reflections from thinly layered poroelastic reservoirs, paper presented at 77th Annual International Meeting, Soc. of Explor. Geophys., San Antonio, Tex.

Quintal, B., S. M. Schmalholz, and Y. Y. Podladchikov (2009), Low-frequency reflections from a thin layer with high attenuation caused by interlayer flow, *Geophysics*, *74*, N15–N23, doi:10.1190/1.3026620.

Rapoport, M. B., L. I. Rapoport, and V. I. Ryjkov (2004), Direct detection of oil and gas fields based on seismic inelasticity effect, *Leading Edge*, *23*, 276–278, doi:10.1190/1.1690901.

Rubino, J. G., C. L. Ravazzoli, and J. E. Santos (2009), Equivalent viscoelastic solids for heterogeneous fluid-saturated porous rocks, *Geophysics*, *74*, N1–N13, doi:10.1190/1.3008544.

Shewchuk, J. R. (1996), Triangle: Engineering a 2D quality mesh generator and Delaunay triangulator, in *Applied Computation Geometry: Towards Geometric Engineering*, edited by C. L. Ming and M. Dinesh, pp. 203–222, Springer, Berlin, doi:10.1007/BFb0014497.

Shewchuk, J. R. (2002), Delaunay refinement algorithms for triangular mesh generation, *Comput. Geom.*, *22*, 21–74, doi:10.1016/S0925-7721(01)00047-5.

Strang, G. (1986), *Introduction to Applied Mathematics*, Wellesley-Cambridge Press, Wellesley, Mass.

Toms, J., T. M. Müller, R. Ciz, and B. Gurevich (2006), Comparative review of theoretical models for elastic wave attenuation and dispersion in partially saturated rocks, *Soil. Dyn. Earthquake Eng.*, *26*, 548–565, doi:10.1016/j.soildyn.2006.01.008.

Vogelaar, B., D. Smeulders, and J. Harris (2010), Exact expression for the effective acoustics of patchy-saturated rocks, *Geophysics*, *75*, N87–N96, doi:10.1190/1.3463430.

Wenzlau, F., and T. M. Müller (2009), Finite-difference modeling of wave propagation and diffusion in poroelastic media, *Geophysics*, *74*, T55–T66, doi:10.1190/1.3122928.

Wenzlau, F., J. B. Altmann, and T. M. Müller (2010), Anisotropic dispersion and attenuation due to wave-induced fluid flow: Quasi-static finite element modeling in poroelastic solids, *J. Geophys. Res.*, *115*, B07204, doi:10.1029/2009JB006644.

White, J. E. (1975), Computed seismic speeds and attenuation in rocks with partial gas saturation, *Geophysics*, *40*, 224–232, doi:10.1190/1.1440520.

White, J. E., N. G. Mikhaylova, and F. M. Lyakhovitskiy (1975), Low-frequency seismic waves in fluid-saturated layered rocks, *Izv. Acad. Sci. USSR Phys. Solid Earth*, Engl. Transl., *11*, 654–659.

Zener, C. (1948), *Elasticity and Anelasticity of Metals*, Univ. of Chicago Press, Chicago, Ill.

Zhu, X., and G. A. McMechan (1991), Numerical simulation of seismic responses of poroelastic reservoirs using Biot theory, *Geophysics*, *56*, 328–339, doi:10.1190/1.1443047.

Zienkiewicz, O. C., and T. Shiomi (1984), Dynamic behavior of saturated porous media; the generalized Biot formulation and its numerical solution, *Int. J. Numer. Anal. Methods Geomech.*, *8*, 71–96, doi:10.1002/nag.1610080106.

Zienkiewicz, O. C., and R. L. Taylor (1989), *The Finite Element Method*, McGraw Hill, New York.

Zienkiewicz, O. C., A. H. C. Chan, M. Pastor, B. A. Schrefler, and T. Shiomin (1999), *Computational Geomechanics With Special Reference to Earthquake Engineering*, John Wiley, New York.

M. Frehner, Department for Geodynamics and Sedimentology, University of Vienna, Universitätszentrum Althanstrasse, Althanstr. 14, A-1090, Vienna, Austria. (marcel.frehner@univie.ac.at)

B. Quintal, Department of Earth Sciences, ETH Zurich, Sonneggstr. 5, CH-8092, Zurich, Switzerland. (beatriz.quintal@erdw.ethz.ch)

S. M. Schmalholz, Institute of Geology and Paleontology, University of Lausanne, Bâtiment Anthropole, CH-1015, Lausanne, Switzerland. (stefan.schmalholz@unil.ch)

H. Steeb, Mechanics–Continuum Mechanics, Ruhr-University Bochum, Universitätsstr. 150, D-44780, Bochum, Germany. (holger.steeb@rub.de)